



MASTER PROJECT

Nonlinear dynamic analysis of steel moment resisting
frames with highly inelastic panel zones

Student

Damien Balmer

Supervisor

Prof. Dr Dimitrios Lignos

Advisor

Dr. Andronikos Skiadopoulos

Tianyu Gu

Ce Wen

July 2023

TABLE OF CONTENTS

1	Abstract	1
2	Introduction	2
3	Methodology	5
4	Archetype building	6
5	Earthquake signal analysis	11
6	Building modelling	13
6.1	Material model	13
6.2	Part geometry and meshing	13
6.2.1	Beams and columns	13
6.2.2	Continuity plate	16
6.2.3	Doubler plate	16
6.2.4	Beam-column-joint	18
6.3	Constraints	18
6.4	Boundary condition	19
6.5	Mass and loads	20
6.6	Strong panel zone design	20
7	First story model validation	22
7.1	Push-over analysis	22
7.1.1	Lateral stiffness derivation	22
7.1.2	Shear distortion	26
7.1.3	Beam chord rotation	27
7.1.4	Top column chord rotation	28
7.1.5	Story drift validation	28
7.1.6	Interior panel zone equilibrium	29
7.1.7	Panel zone shear force	30
7.2	Dynamic analysis	34
8	Eight story building results	40
8.1	Frequency analysis	40
8.2	Dynamic analysis	41
9	Conclusion	45
10	Acknowledgment	46
11	Data availability	46
12	Appendix	49
12.1	Design Summary	50

1 Abstract

This study focuses on the stability assessment of a steel moment-resisting frame (MRF) with a high panel zone design shear distortion demand. An archetype building prone to shear buckling issues in the panel zone was selected as the subject of investigation. The entire building was accurately modeled using the continuum finite element software Abaqus. The methods employed to compute the different components of deformation (shear distortion, chord rotation) and to determine the force demand were derived and validated through static push-over and dynamic analyses on a single-story structure.

The analysis compared two structural designs, highlighting the advantages of a weak panel zone design. The weak panel zone design exhibited a higher proportion of inelastic deformation in the panel zone, resulting in reduced demands on columns and beams. No buckling occurred in the panel zone up to shear distortions of 5.6 times the yield shear distortion, whereas flexural buckling was observed in the strong panel zone design.

The behavior of the panel zone was studied, and the simulation results aligned well with the stiffness of the Skiadopoulos et al., 2021 model. However, discrepancies emerged in the post-yield range, likely due to the more complex stress state considered in the simulation and the location of shear distortion measurement points. The proposed panel zone model showed an improved description of the panel zone elastic stiffness compared to the commonly used engineering practice model.

Although this master thesis provides valuable insights into the system-level behavior associated with a weak panel zone design and numerical simulations, limitations regarding the full-building model and convergence issues were encountered. Future work should address these issues by modifying solver or model parameters. Furthermore, the influence of composite action on panel zone behavior, not considered in the proposed model, should be investigated in future studies.

2 Introduction

Frame structures are a fundamental type of construction used in buildings. They consist of interconnected beams and columns in a two-dimensional series. Frame structures are popular due to their structural, aesthetic, and functional advantages. A range of materials are utilized in constructing frame structures, such as steel and reinforced concrete. Steel has exceptional material performance in terms of stiffness and strength, enabling the creation of lightweight structures. The first skyscraper, designed by William LeBaron Jenney in 1885, was constructed using a steel skeleton structure, paving the way for an era of tall buildings.

Moment-resisting frames MRFs are special frames where beam-to-column joints possess sufficient stiffness to maintain the original angle between the members. Beam-column joints, often denominated, as panel zones, is the column web area delineated by the extension of beam and column flanges through the connection (AISC, 2016c). These joints are comprised of welded or bolted connections. These frames are designed to carry vertical and horizontal loads such as wind or inertia forces induced by earthquakes. They can be positioned in the perimeter of the structure or in the interior, connection can be made between two orthogonal frames to produce a 3D structure. MRFs provide large architectural versatility compared to braced frames or shear walls. These structures are particularly appreciated because large open spaces can be created for different types of building use. The structural system is suitable for low to mid-rise structures. In fact, framing systems tend to be inefficient in high-rise buildings due to their relatively low lateral stiffness compared to other structural systems (braced structure).

When it comes to the design of the lateral force-resisting system LFRS, engineers have access to two approaches. The old and popular approach is the force-based design. Force-based design is a design approach that involves analyzing structures for their response to different loads and forces, such as wind or seismic forces, and designing them to resist those forces by considering the distribution of forces throughout the structure. This design approach typically involves calculating the forces that the structure is likely to experience and then designing the components of the structure to resist those forces, while ensuring that the structure remains stable and functional.

On the other hand, displacement-based methods for steel structures appeared in the 2000s (Medhekar & Kennedy, 2000). The structure is designed for a targeted displacement during an earthquake. An effective stiffness is retrieved from a push-over analysis of the structure. Given the stiffness and the mass, the effective (inelastic) period of the structure is retrieved. The maximum allowable displacement of the structure is finally compared to the displacement given by the displacement spectrum. This method provides better control of the level of damage after an earthquake. However, engineers tend not to use it in practice, because this method requires multiple design iterations.

Capacity design is considered an essential tool for controlling inelastic response in force-based design for ductility. A historical review traces back the origin of capacity design in (Fardis, 2018). The theoretical concept was first laid out in 1961 (Blume, 1961) and came to the attention of a broad international audience in 1991 (Park & Paulay, 1991). Its purpose is to direct the global displacement demand and total energy input to those components of the system that are easy to inspect and repair and are less critical for the stability of other components or the integrity of the system. By establishing a hierarchy of components, a sequence is determined for when they will enter the inelastic range during the response to a ground motion. Components that meet the criteria for being ductile are then proportioned to have force resistance at least equal to the corresponding force demand from an elastic analysis under a reduced seismic action. Non-ductile components are proportioned to remain elastic before and after the ductile components enter the inelastic range.

When it comes to design philosophy, as in AISC, 2016b, a distinction between 3 types of MRF is made based on the ductility of the structure. Ordinary moment frames provided minimal inelastic deformation capacity in their members and connections. The intermediate moment frame provided limited inelastic deformation capacity through flexural yielding of the beams, columns, and shear yielding of the column web panel zone. Finally, special moment frames provide considerable inelastic deformation capacity through significant flexural yielding of the beams and limited shear yielding of the column web panel zone. Moreover, columns are

designed to be stronger than fully yielded and strain-hardened beams. The flexural yielding of the base end of the column is permitted.

When designing, a structure to resist lateral loads, it is important to control the sway of the buildings. Such verification is often conducted through the story drift ratio SDR, representing the lateral deflection of a story over its height. This limit serves to maintain a certain level of service after design base earthquake DBE and prevents failure after maximum considered earthquake MCE. The lateral deflection of an MRF structure is three-folded, it consists of a flexural, shear, and axial deformation component. The first is prominent, as the beam-to-column joint is rigid, and the lateral deflection of the columns induced flexion in the beams. Second, the shear deflection in the beams and columns provides relative flexibility to the structure. In the current design practice, the shear distortion of the panel zone participates in a moderate way to the story rotation. Finally, axial deformation is often neglected due to the high axial rigidity of the members. However, the axial deformation of the columns can be significant in the case of tall buildings. The transient axial forces induced by lateral loads sustained by the columns lead to non-negligible axial elongation and shortening.

The earthquake that struck Northridge on January 17, 1994, was a significant event with a moment magnitude of 6.7 Mw. It caused peak ground acceleration of up to 1.8g in the horizontal plane and resulted in extensive damage to various structures in the neighboring city of Los Angeles, including bridges, lifeline facilities, residential buildings, and commercial structures (Yegian et al., 1995). The most concerning aspect of the damage was observed in the beam-to-column connections of steel moment-resisting frames (MRFs). The severity of the damage raised doubts about the predictability of steel MRF behavior and the reliability of conventional connections used in California buildings over the previous two decades (Youssef et al., 1995). Consequently, extensive investigation campaigns were initiated, leading to several key findings.

Firstly, it became apparent that low-probability earthquakes, such as the Northridge and Kobe earthquakes, could have a significant impact on structures, resulting in substantial structural damage and high repair costs. This realization emphasized the need for a better understanding of seismic behavior and improved design practices. Secondly, large-scale experimental testing campaigns were undertaken to gather valuable data and insights. These tests aimed to simulate and study the effects of seismic forces on structural components and connections, helping researchers and engineers develop more robust and resilient designs. Furthermore, the investigation focused on the connections used before the Northridge earthquake. It was discovered that the beam-flange welding rupture was primarily caused by the triaxial stress state developed at the beam-flange to column-flange location. This stress state led to a less ductile behavior compared to uniaxial steel coupon testing. Additionally, it was found that the mechanical properties of the steel were not conservatively determined, with a significant portion falling below the design values. Flaws were also present in the welds due to inappropriate welding specifications, and the geometry of the welding access holes caused high-stress concentration in the beam flanges. Moreover, shear distortions in the panel zone, create a high-strain state at panel zone kinking locations. The combination of these factors ultimately resulted in a brittle fracture in the beam flange region (Paul Popov et al., 1998).

To address these issues, new welding specifications were implemented. Two cost-effective solutions were proposed: the removal of the backing bar with a carbon arc and the application of a fillet weld. The first solution proved to be more expensive, while the second option, applying a fillet weld at the bottom of the backing bar to induce a center crack away from the edges, was found to be more cost-effective. Additionally, new beam-to-column connection designs such as the dog-bone connection, or reinforced corner plate were introduced to shift the plastic hinge away from the column face. Overall, the extensive investigations and subsequent implementation of improved welding specifications and connection designs have significantly enhanced the seismic resilience of structures. However, one major drawback of these specifications has been the limitation on the panel zone shear demand. In fact, in modern specifications, the shear resistance of the panel zone is limited in order to avoid panel zone kinking

As above mentioned, the involvement of beam-to-column web panel zones in energy dissipation during earthquakes is often limited. As a result, beam local buckling can occur even at relatively low lateral drift demands, leading to significant structural repair costs after seismic events. This design practice is primarily influenced

by two factors. Firstly, it is driven by the recognized limitations of panel zone design models, which hinder our ability to effectively balance the seismic design of fully restrained beam-to-column connections. These limitations pose challenges in accurately predicting and accommodating the behavior of panel zones under seismic forces. Secondly, the avoidance of panel zone participation in energy dissipation is also influenced by concerns related to panel zone kinking, which has the potential to increase the likelihood of fracture in beam-to-column connections. This risk is taken into account to ensure the integrity and durability of the connections.

In the literature, several models have been developed to simulate the behavior of inelastic panel zones in terms of shear strength, V_{pz} , and shear distortion angle, γ . These models include contributions from (Fielding & Huang, 1971), (Kim & Engelhardt, 2002), (Krawinkler, 1978). These models consist of elastic stiffness, K_e , dominated by shear deformation mode up to the yield shear strength, V_y . This assumption is based on a uniform distribution of shear stress in the column web. The models also incorporate an inelastic hardening branch characterized by a post-yield stiffness (K_p), representing the panel zone's behavior after yielding up to a shear strength, V_p at $4\gamma_y$. This shear strength accounts for the contribution of surrounding elements such as continuity plates and column flanges. Additionally, these models typically include a third branch where the shear strength is assumed to stabilize. The post- γ_p slope of this branch is expressed as a percentage of the elastic stiffness and is discussed further in subsequent analyses. In the current provision, the shear force demand in the panel zone is limited to its plastic resistance, design shear distortion, γ_d , is thus limited to $4\gamma/\gamma_y$ (AISC, 2016c).

Highly inelastic panel zones have shown favorable behavior in seismic analysis (Lee et al., 2005). The development of an inelastic panel zone database has provided valuable insights (Skiadopoulos & Lignos, 2021). The database revealed deviations between current panel zone models and measured data, including discrepancies in stiffness and strength. Additionally, the database offers a range of shear distortions in the panel zone that can withstand lateral drift demands greater than 4% without experiencing premature beam flange fracture. To address these limitations, accurate panel zone models have been proposed as replacements for outdated code models (Skiadopoulos et al., 2021). The proposed model takes into account the specific requirements of slender panel zones, accurately considers doubler plate effects, and incorporates axial-load strength reduction.

System-level simulations conducted on SMRF with weak panel zone designs have yielded promising results (Skiadopoulos & Lignos, 2022). These simulations have shown that structures featuring weak panel zones perform well, sometimes even better than those with strong panel zones. The mean annual frequency of collapse for such structures is up to two times lower than that of code-compliant MRFs. Additionally, a 50% reduction in SDR at DBE level compared to code-compliant MRFs has been observed. The beam-to-column joints in weak panel zone designs do not experience a premature fracture due to panel zone kinking. Moreover, the occurrence of local buckling in steel beams is significantly limited, even under MCE. This study has significant implications for seismic design and the post-seismic reparability of steel MRFs.

(Skiadopoulos & Lignos, 2022) highlight the high computational cost of a full-continuum model compared to a beam-column element model. Research into limiting the number of degrees of freedom has been undertaken. The use of finite elements of different dimensions makes it possible to greatly reduce the size of a model. In areas of interest, high-precision finite elements are used, while coarser elements are chosen for the rest of the model. Shim et al., 2002 offers a method for coupling solid elements to beam elements, for example. Advanced commercial softwares are equipped with in-built multiple-point constraints (MPC) enabling such coupling. However, (Hartloper et al., 2022) addresses the limitation of the above-mentioned coupling method by proposing new constraint equations formulation for transmitting warping between elements. A subroutine is available for implementing MPC in Abaqus. Another way of simply reducing the size of a model is to work with an equivalent static system, as shown in (Islam & Imanpour, 2023).

Performance during the non-linear analysis described in Skiadopoulos and Lignos, 2022 has ensured adequate behavior of structures subject to a variety of earthquakes. However, the simulations carried out so far do not consider global or local imperfections in beams and columns. These imperfections are crucial in analyzing the stability of structural components. In particular, the simulations involving weak panels in Skiadopoulos

and Lignos, 2022, only consider the strength aspect as no imperfection is input in the employed panel zone model (Skiadopoulos et al., 2021).

The aim of this Master’s project is to pursue the above-mentioned research by addressing the analysis of structural stability, particularly in the panel zones. The objective of this study is to assess the stability of a steel MRF featuring high panel zone shear design demand ($\gamma_d = 10\gamma_y$) subjected to a real earthquake ground motion. To fulfill the objective of this study, a nonlinear time-history analysis of an 8-story steel MRF is conducted, and the stability of the structure is assessed employing various EDP. However, to provide the reader with the assurance of the correct analysis of the structure, two validation steps are provided. In these two steps, the analysis structure consists of the first story of the building. Firstly, a push-over analysis validates the force consideration and the story rotation component computation. Secondly, a dynamic analysis is performed to validate the consideration of dynamic effects employing the same method as in the push-over analysis. Furthermore, the response of a weak and strong panel zone design is compared. Finally, the eight-story building simulation is conducted and the results are provided.

3 Methodology

This section presents the general methodology for achieving the goal of this master’s thesis, as described in the previous section.

Firstly, an archetype building designed in Skiadopoulos and Lignos, 2022, is chosen based on its susceptibility to shear buckling in the panel zone. The building beam, and columns cross-sections, loads, and mass are defined. An earthquake ground-motion acceleration signal is selected. The building is modeled using Abaqus version 2019 (Smith, 2019). To reduce the overall size of the computational finite element (CFE) model, two methods are employed. Firstly, a static equivalent substructure is utilized as in (Islam & Imanpour, 2023), representing half of the archetype building’s MRF. Secondly, instead of implementing continuum finite elements throughout the entire model, they are selectively incorporated only in zones where yielding or stability issues are expected. For zones exhibiting elastic behavior, beam-column elements are employed. The connection between domains of different dimensions is achieved using special multiple-point constraints (Hartloper et al., 2022). Global and local imperfections are inputted in the beam and columns, whereas geometric imperfections are not implemented in the panel zones.

Validation of the computation of various EDP is done through a push-over analysis and a dynamic analysis of the first story. Moreover, a comparison between a strong panel zone design (current practice, AISC, 2016b) and a weak panel zone design ($\gamma_d \geq 4\gamma_y$) is provided. Finally, the non-linear response history analysis (NLRHA) of the eight-story building is analyzed.

4 Archetype building

In this report, an archetype steel office building is employed. Prior work (Skiadopoulos, 2022), performed nonlinear static and dynamic analysis on 32 archetype steel office buildings. For the purpose of this report, one archetype building has been selected. The selected design is considered to be relevant regarding the study of shear buckling of the panel zone, as it exhibits the lower shear buckling critical stress, $\tau_{cr}/\tau_y=1.27$ (subsection 12.1)

The design developed in (Skiadopoulos, 2022) consists of an 8-story 5-bay. A soil class D and a risk category II are assumed. The design location is urban California. The lateral restraints systems comprised two concentrically braced frames and two special moment resisting frames in the N-S and E-W directions, respectively. The typical story height is 4.0m and the first-floor story height is equal to 4.2m. Figure 1 and Figure 2 depict the plan view and the elevation of the building. The analysis of this report focuses on the building response in the N-S direction. All steel components are made out of A992 Gr50 steel. The initial design from (Skiadopoulos, 2022) considered yield stress $f_y = 345 \text{ MPa}$. In this report, the yield stress, $f_y = 379.5 \text{ MPa}$, led to changes in the doubler plate thicknesses (see subsection 12.1). A 100mm thick concrete slab lies on a 90mm thick steel deck. The beam-to-column ties are made out of pre-qualified WUF-W.

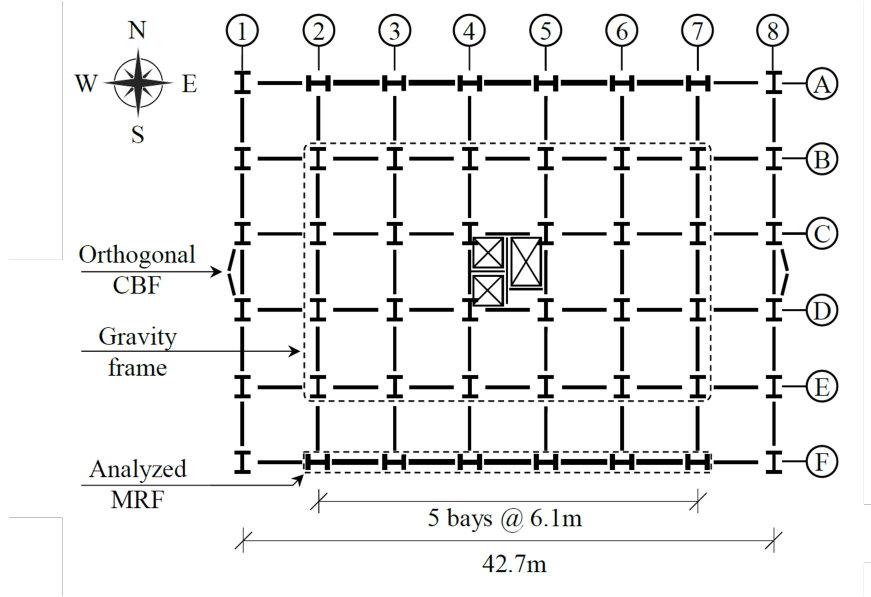


Figure 1: Plan view of the five-bay steel MRF (Skiadopoulos, 2022)

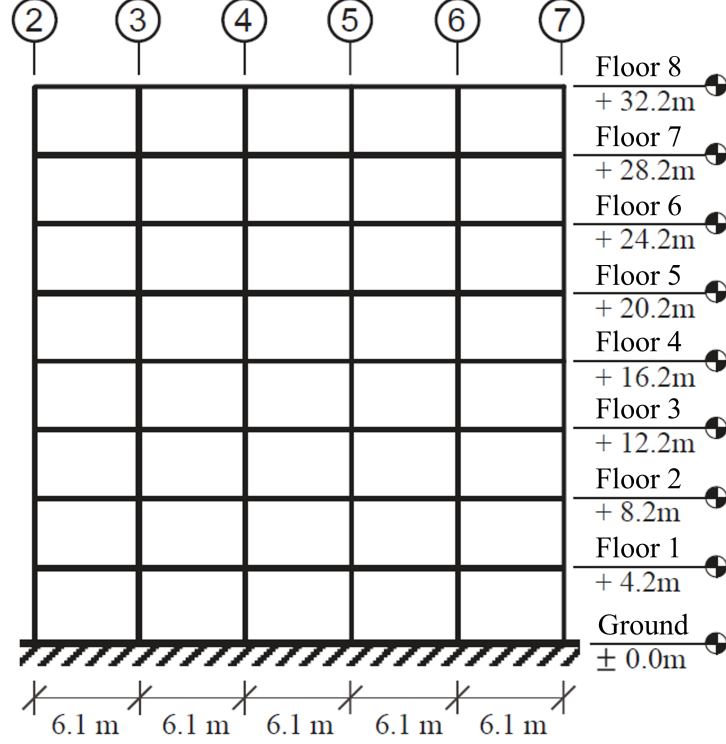


Figure 2: Elevation of the eight-story five-bay steel MRF (modified figure from Skiadopoulos, 2022)

The beam-to-column web panel zones are designed to exhibit a high level of inelastic deformation. The targeted panel zone shear distortion is equal to $\gamma_d = 10\gamma_y$. This high level of shear distortion is yet not permitted in the AISC 360-16. The ratio between the panel zone shear resistance, R_n (AISC 2016c), over the panel zone shear demand, R_u (AISC 2016b) is equal to 0.84. The fundamental structure period, T_1 is equal to 2.12s. The column and beam cross-sections dimension are reported in Figure 3. Column splices are located at a mid-story height, Figure 3 reports the column and beam cross-section assignments. The exterior columns do not have doubler plates. The MRF is designed with a response modification factor, $R = 8$, an overstrength factor, $\Omega_0 = 3$ and a deflection amplification factor, $C_d = 5.5$.

Columns	depth	width	flange thickness	web thickness	fillet radius
	d_c	b_{cf}	t_{cf}	t_{cw}	r
	[dm]	[dm]	[dm]	[dm]	[dm]
W 24x62	6.0300	1.7880	0.1500	0.1080	0.1270
W 24x84	6.1200	2.2900	0.1960	0.1180	0.1270
W 24x94	6.1740	2.3020	0.2220	0.1300	0.1270
W 24x104	6.1100	3.2380	0.1900	0.1260	0.1270
W 24x131	6.2180	3.2640	0.2440	0.1540	0.1020
Beams	depth	width	flange thickness	web thickness	fillet radius
	d_b	b_{bf}	t_{bf}	t_{bw}	r
	[dm]	[dm]	[dm]	[dm]	[dm]
W 18x55	4.6000	1.9120	0.1600	0.0980	-
W 21x62	5.3300	2.0920	0.1560	0.1020	-
W 21x73	5.3940	2.1060	0.1880	0.1160	-
W 24x76	6.0760	2.2820	0.1720	0.1120	-

Figure 3: Column and beam cross-section. Values transformed from inches to decimeters with rounding to the 0.002 nearest multiples. The fillet radius of the beams is not modeled.

Story	IC	EC	Beam	DP
8	24x84	24x62	18x55	5/16
	SPLICE			
7	24x94	24x62	18x55	5/16
		SPLICE		
6	24x94	24x84	21x62	6/16
	SPLICE	SPLICE		
5	24x104	24x104	21x62	6/16
4	24x104	24x104	21x73	8/16
	SPLICE	SPLICE		
3	24x131	24x131	21x73	8/16
2	24x131	24x131	24x76	6/16
1	24x131	24x131	24x76	7/16
0	GROUND	GROUND	GROUND	GROUND
SPLICE	column splice at mid-story height			
DP	doubler plate, in inches			
IC	interior column			
EC	exterior column			

Figure 4: Eight-story five-bay MRF design. Doubler plate thicknesses in inches. The doubler plate thicknesses are rounded to the 0.002 nearest multiples in decimeters.

The MRF is designed considering:

- P- Δ effects by leaning column modeling
- The panel zone contribution to the MRF deformation
- Physical dimension of beams and columns
- Response spectrum analysis (RSA)

The considered loads are the following:

- Dead load: 4.3 kN/m^2
- Live load floor: 2.4 kN/m^2
- Dead load roof: 0.96 kN/m^2
- Cladding: 1.2 kN/m^2
- Earthquake load: design spectrum

The seismic mass is computed by considering the characteristic values of the dead loads acting on the MRF (cladding and floor dead load). Each floor is made out of 6 masses that are located on each column (see Figure 6). The tributary area of one frame is depicted in blue in Figure 5. Table 1 provides the value of the seismic masses.

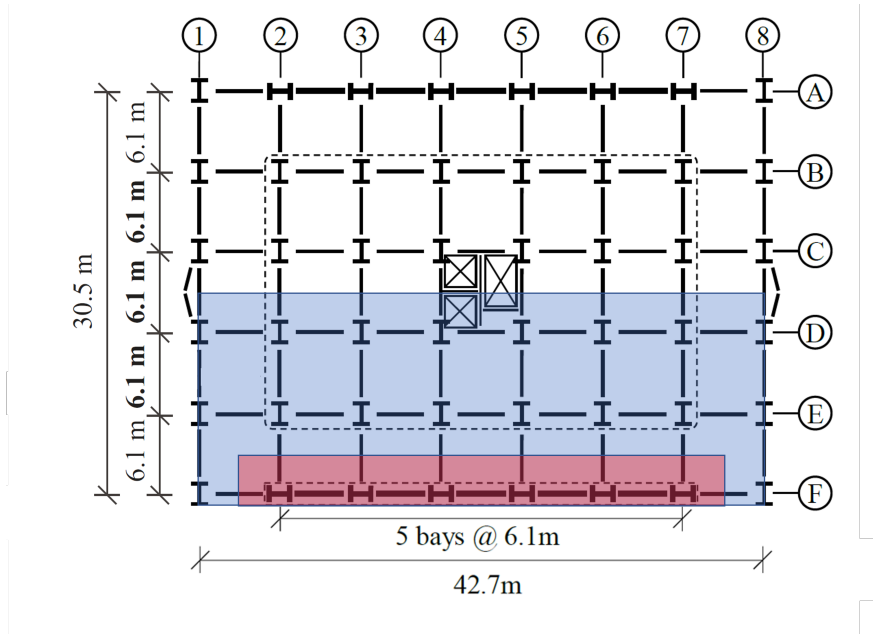


Figure 5: Tributary area of one frame (blue) and tributary of the MRF columns (red). (modified figure from Skiadopoulos, 2022)

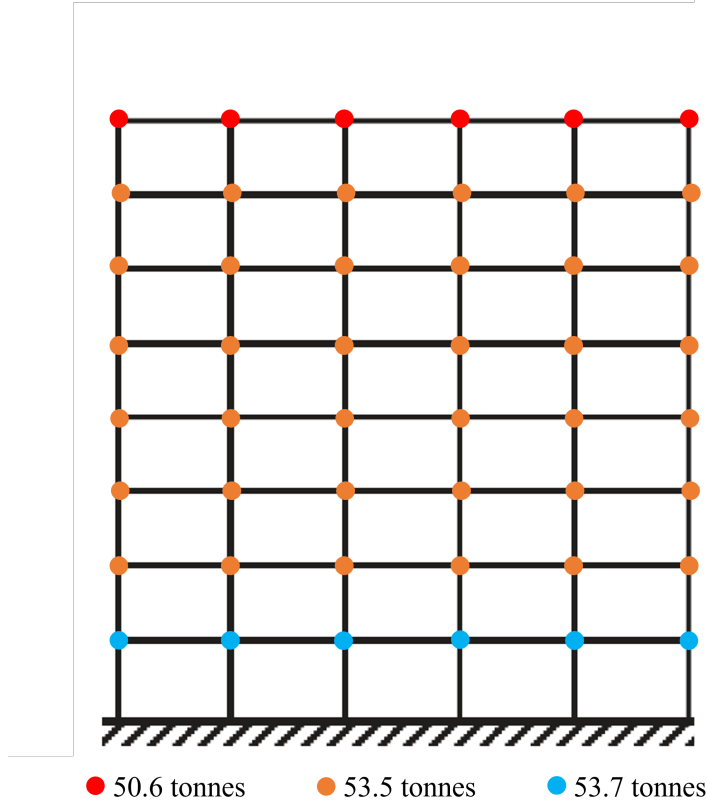


Figure 6: Lumped mass repartition through the structure

Roof mass [kgtonnes]	Typical story mass [kgtonnes]	1st floor mass [kgtonnes]
50.6	53.5	53.7

Table 1: Seismic masses disposed at each story column.

The MRF's column axial load, N_d is computed according to the tributary area shown in Figure 5 using the following combination

$$N_d = 1.05 \cdot DL + 0.25 \cdot LL$$

With the dead loads, DL , and the live loads, LL . Figure 5 show the tributary area of the 6 MRF columns. The dead load and live load factor are taken from Skiadopoulos, 2022 which is in accordance with ASCE-7 22. Table 2 summarizes the axial load acting on each column.

	Roof load [kN]	Typical story load [kN]	1st floor load [kN]
MRF column	110.5	125.9	126.7
Leaning column	1297.6	1444.2	1446.5

Table 2: Axial load on each column and the leaning column

5 Earthquake signal analysis

The studied event is the Northridge earthquake ($M_w = 6.7$), which happened the morning of the 17th of January 1994. The signal duration differs from the record station but is in the range of 10 to 20 s. It is a blind-thrust earthquake, meaning that the thrust is not visible at the surface. The event was felt in big cities of California such as Los Angeles and San Diego.

The earthquake ground motion employed in the simulation is the ground acceleration record of the Canoga Park Epiphany Lutheran Church at 19.9 km from the hypocenter. The acceleration record was downloaded from (“COSMOS: Northridge 1994-01-17 12:30:55 UTC”, n.d.). The record is characterized by a peak ground acceleration, $PGA = 0.36g$, and a peak ground displacement, $PGD = 6.8cm$. Figure 7 shows the acceleration record.

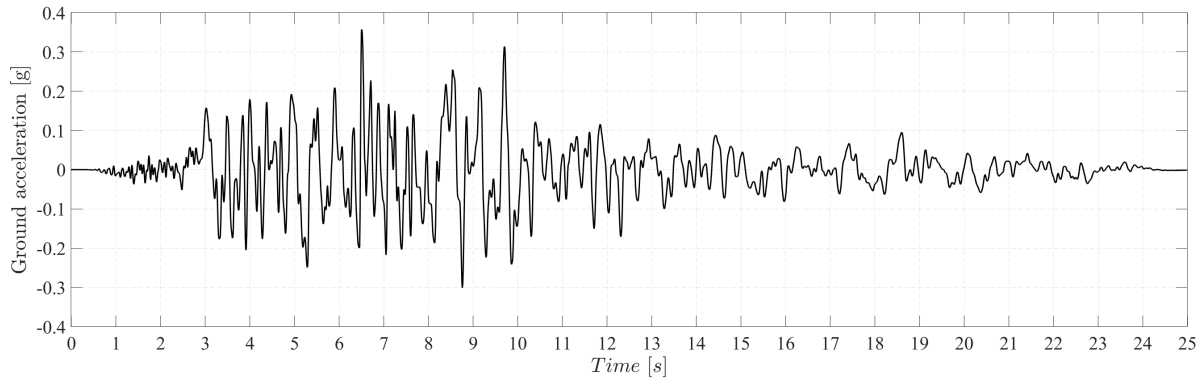


Figure 7: Ground motion acceleration record, Canoga Park CA, Epiphany Lutheran Church, 19.9 from the hypocenter

In this report, a scaled 1.5 version of the original earthquake is also employed. Figure 8 shows the 5% damping elastic spectrum. An elastic displacement considering the scaled earthquake, between 11 and 38 cm is expected for the structural period range between 1 and 2.5s respectively.

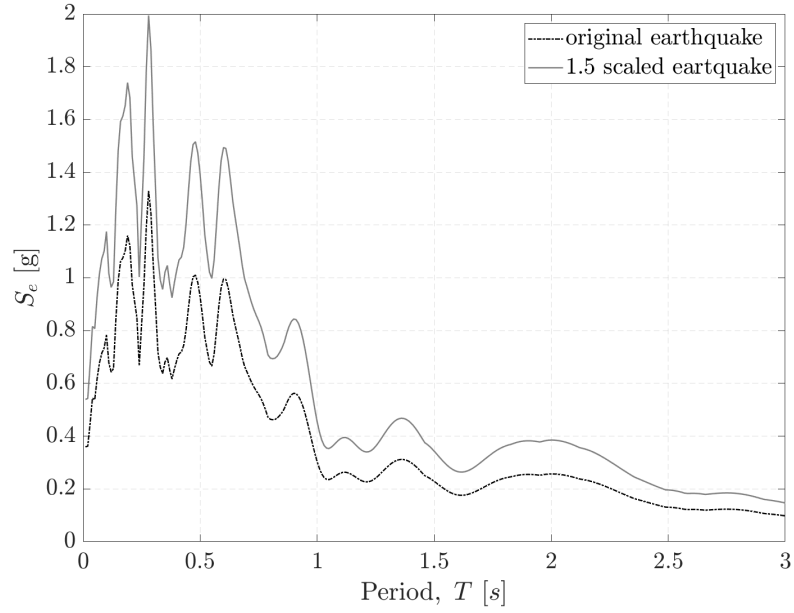


Figure 8: Elastic acceleration spectrum with 5% damping for the original and the 1.5 scaled earthquake

6 Building modelling

6.1 Material model

To capture plastic non-linearities, and kinematic and isotropic hardening of structural steel as close as possible to actual behavior, the UVC material model is used from (Hartloper et al., 2021). All parts of the building model are made out of A992 Gr50 mild steel. Table 3 summarizes the employed parameters of the UVC material model. The parameters are taken from (Hartloper et al., 2021). Note that the young Modulus, $E = 210 \text{ GPa}$, and the specified minimum yield stress, $f_{y,min} = 345 \text{ MPa}$ complies with the AISC, 2016b and are not the original value of (Hartloper et al., 2021). Moreover, the expected yield stress, f_y , is taken in accordance with AISC, 2016b, ($R_y = 1.1$).

E	$f_{y,min}$	f_y	Q_∞	b	D_∞	a	C_1	γ_1	C_2	γ_2
<i>GPa</i>	<i>MPa</i>	<i>MPa</i>	<i>MPa</i>	-	<i>MPa</i>	-	<i>MPa</i>	-	<i>MPa</i>	-
210	345	379.5	141.47	15.2	135.95	211.16	25621	235.12	942.18	3.16

Table 3: UVC material model parameters. (Hartloper et al., 2021)

The implementation into Abaqus is done through a UMAT. It is a user subroutine to specify material mechanical behavior developed by (Hartloper et al., 2021). Uniaxial UMAT is employed for beam elements and multiaxial UMAT is employed for solid elements.

6.2 Part geometry and meshing

The model is made out of five generic components which are:

- Columns
- Beams
- Continuity plate
- Doubler plate
- Beam-column joint

There are 4 types of finite element

- 2-node linear open section beam in space (B31OS)
- 2-node linear 3-D truss. (T3D2)
- 8-node linear brick, reduced integration, hourglass control (C3D8R)
- 6-node linear triangular prism (C3D6)

Moreover, a viscosity factor of 1% is set on the solid element to help the convergence. In the following sections, the modeling of each component will be detailed. The purpose of these explanations is to clarify the geometrical and meshing assumptions.

6.2.1 Beams and columns

To limit the number of nodes in the model, columns, and beams are modeled in three distinct parts, with two solid elements at each end and a central beam element. In the latter, only elastic deformation is expected. In the other two parts, however, the use of solid elements enables the occurrence of plastic deformations to be analyzed with greater precision. The extent of the solid element domains is dictated by the zone where such plastic deformation would be expected. Sensitivity analyses made by Hartloper, 2021 have shown that

a length of $1.5d$ (depth of the member cross-section) produces results of comparable quality to a model composed exclusively of continuous elements. In the case of columns, this length is reduced to expect a value of around $1.25d$. This modification is necessary because the doubler plate extends 150 mm above and below the beam flanges. In fact, the doubler plate cannot be in contact with the column, for reasons of incompatibility linked to the introduction of geometrical imperfections in the columns. The continuous domain could then have been extended, but given the general size of the model, it's important to try and limit the number of nodes.

Imperfections are introduced in the mix-dimension macro-elements using the `pywikc` module to generate imperfection files for the members (see Figure 9). These imperfections consist of a global imperfection in the out-of-plane direction ($L/1500$), as well as local imperfections in the profile flanges ($b_f/3000$) and web ($d/3000$). The amplitude of these imperfections corresponds to standard manufacturing tolerance values (AISC, 2016c). The extent of the local imperfection buckling wave, L_{bw} extends over the whole continuum domain. For floor columns where the cross-section changes at mid-height, it was not possible to introduce a global imperfection. Insofar as the first instances of these columns appear on the 4th floor, global instabilities in these columns are not expected.

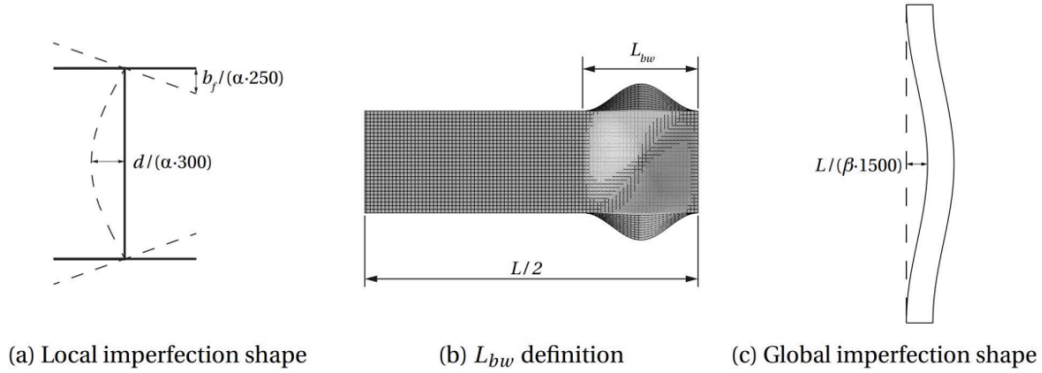


Figure 9: Global and local imperfection (Hartloper, 2021)

The cross-section geometric dimensions of the beams and columns are reported in Figure 4.

The number of beam-column elements per member is set to eight according to Hartloper, 2021 and the global mesh size for solid elements is taken 20 mm. The latter is slightly smaller than the recommended value by Hartloper, 2021, but is intended to better fit the smaller dimensions of the parts. The thickness of the flanges and webs is made up of three elements. In addition, in the column part where the fillet radius between the flanges and the web is represented, the K-area mesh is refined (Figure 10).

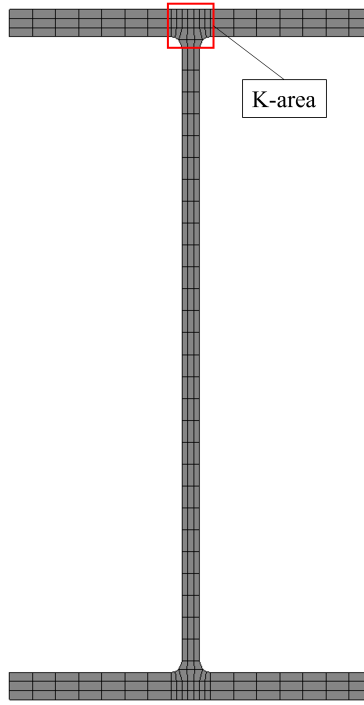


Figure 10: Column cross section mesh (W 24 x 131)

In the beam members, a weld access hole is modeled according to AWS, 2016. The presence of the weld access hole disturbs the hexahedral element mesh. The shape of the zone forces certain elements to be tilted towards 6-node triangular prism elements (C3D6). The beam fillet radius is not modeled to avoid complex geometry due to the presence of the weld access hole. In reality, modeling the weld access hole does not result in the most constraining conditions for the panel zone. This represents a limitation of the present modeling. In fact, it would be more interesting to model the entire cross-section of the beam (fillet radius included) so as to increase the strength of the beam and consequently the shear in the panel zone.

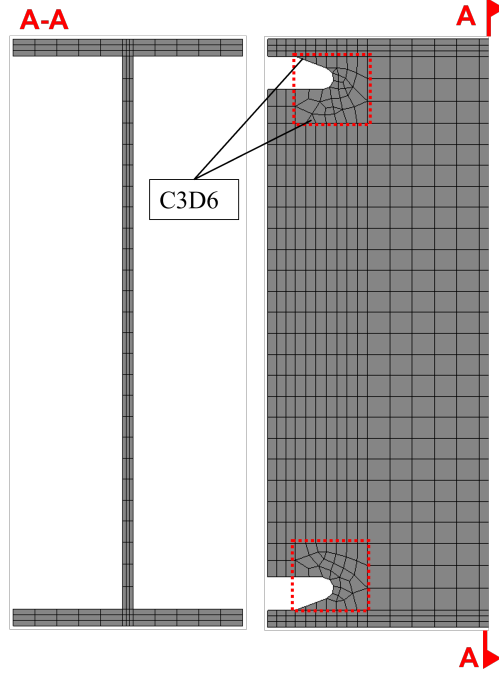


Figure 11: Beam cross section mesh (W 21 x 62) on the left. Elevation view of the member, location of triangular prism element (C3D6)

6.2.2 Continuity plate

The need for a continuity plate is specified in AISC, 2016b. In order to avoid having to calculate the resistance of all column flanges, continuity plates were systematically placed at each beam-column joint. The length of the continuity plates depends on the depth of the column section. The width of the continuity plates is set at the minimum limit provided by AISC, 2016b. The plate extends from the column web to the point opposite the end of the widest beam flange. Corner clips are also required. The dimensions of these corner clips are taken from AWS, 2016. As a result, the welds of the continuity plates are at a distance from the K-area. The reader will notice that the corner clip dimensions differ to take into account the extra thickness of the doubler plate (see Figure 13).

The thickness of the plates is equal to the thickness of the beam flange, t_{bf} . The minimum dimensions required by AISC, 2016b for this thickness is $0.5t_{bf}$ and $0.75t_{bf}$ for the outer and inner columns respectively and are therefore satisfied.

6.2.3 Doubler plate

The thicknesses of liner plates are given in the table below. Their height and width are determined by the geometry of the panel zone. The width of the doubler plate is equal to the internal distance between the two wings of the column. The height of the doubler plate depends on the total height of the beam. In addition, a 150 mm overhang above and below the beam flanges is provided in accordance with AISC, 2016b (Figure 12).

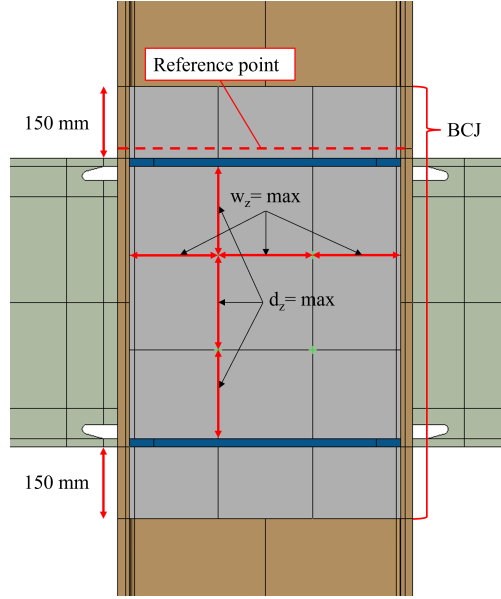


Figure 12: Beam-column joint detail; beam (green), columns (brown), continuity plates (blue). Beam column joint (BCJ). Doubler plates overhang above and below beam flanges (grey) and positioning of the plug-welds. Rigid body-constraint between the reference point and cross-section of the column (red dashed line)

So that the total thickness of the doubler plate can be taken into account in the strength of the web panel, plug-welds must be made in accordance with AISC, 2016b. Plug-weld positioning has been checked using the following formula.

$$t \geq \frac{w_z + d_z}{90}$$

Where t is the individual thickness of the column web or the doubler plate, w_z and d_z are the maximum horizontal and vertical distance between the plug welds or to the end of the panel zone.

The mesh size of the doubler plate is set at 20 mm. The number of elements in the plate thickness corresponds to the number of elements in the radius of the column fillet. When the plate thickness is greater than the fillet radius, additional partitioning is performed at the end of the fillet (see Figure 13). The mesh density of the doubling plate could be increased compared to that of the column core. Indeed, the mesh density of a slave surface should generally be denser than that of a master surface. In particular, this would facilitate the convergence of contact-related problems.

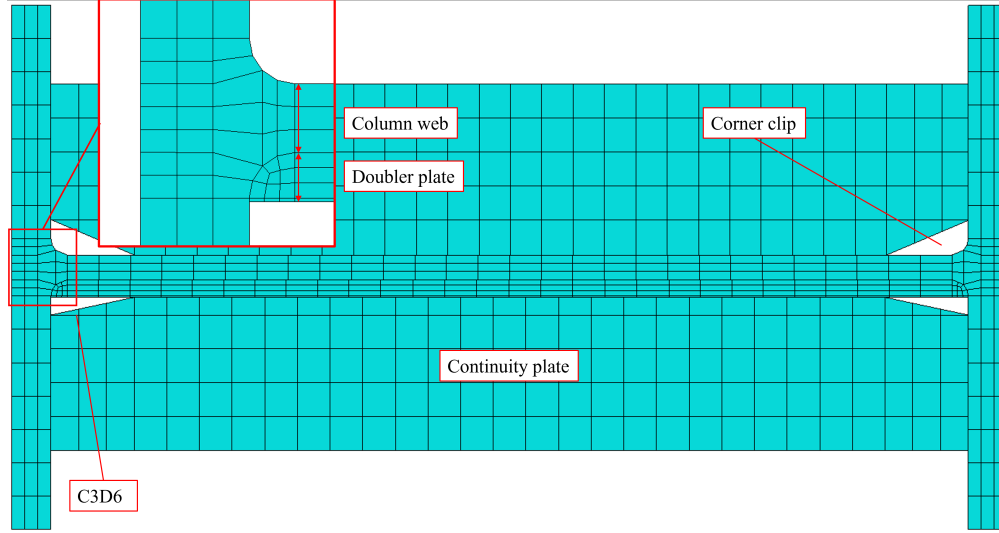


Figure 13: Doubler plate meshing through its thickness. Matching the number of elements at the fillet radius location. Additional thickness partitioning at the end of the fillet radius

Furthermore,

6.2.4 Beam-column-joint

The beam-column joint is a component representing the column in the panel zone. This element has the same properties as adjacent columns (mesh, cross-section). Its individual existence is linked to the compatibility of initial geometric imperfections. These imperfections are generated for each component (beam/column) using the pywikc module (Hartloper et al., 2022). However, in the connection area between beams and columns, it is desirable to have perpendicular connections between the various members. The beam-column joint makes this possible, as no imperfections are introduced into this component. The joint dimensions are dictated by the cross-sectional depth of the beams and columns. In addition, the vertical dimensions of the joint must be extended to coincide with the doubler plate height, for deformation compatibility issues (see Figure 12).

6.3 Constraints

In this section, the constraints governing behavior between parts are discussed. The interactions between the different parts are listed in Table 4, along with their type of constraint.

For simplicity's sake, the welds linking the various components are represented by tie constraints, bearing in mind that the aim of this work is to analyze a system response. The TC links all the degrees of freedom of the slave nodes to those of the master nodes.

The rigid body constraints link one reference point to a node-set or a surface. The node belonging to the slave node follows the same displacement as the reference point. This type of constraint is employed to apply concentrated force/boundary conditions to a surface instead of a single node.

The interaction between the doubler plate and the column web is represented by surface-to-surface contact (SSC). This defines a coefficient of friction, $\mu = 0.3$. The two surfaces are free to separate, but cannot penetrate each other. To avoid convergence problems due to contact, a damping factor of 0.01 is added. This damping factor decreases linearly with the relative distance between the two plates. Furthermore, an intentional gap of 0.5mm is left between the doubler plate and the core of the column, enabling faster convergence.

The connection between the structural beam and the hanging column is pinned. Kinematic coupling is used to select the set of DoFs of the two elements to be linked. The connection at the mid-story splice is The

connection between the separate columns is also made using KC, except that this time all the degrees of freedom of the two elements are connected.

The link between the solid and beam-element domains is made with an MPC that allows warpage to be taken into account. Indeed, when this constraint is used with open-section beam elements, warping can be transmitted from the solid domain (Hartloper et al., 2022).

Plug welds are modeled as discrete faster. In the model, this represents a 15 mm radius cylinder of material connecting a point on the doubling plate surface to the opposite column core surface.

	TC	RBC	SSC	KC	WIKC	DF
Doubler plate - Column web			X			
Doubler plate - Column flange	X					
Continuity plate - Column web	X					
Continuity plate - Column flange	X					
Continuity plate - Doubler plate	X					
BCJ - Column	X					
BCJ - Beam	X					
Column (beam-solid)					X	
Beam (beam-solid)					X	
Mid-story spliced columns				X		
Beam - Leaning column (pinned)				X		
Story load/mass introduction		X				
Base column end		X				
Plug-welds						X

Table 4: Constraints defined in the model; tie constraint (TC), rigid body constraints (RBC), surface-to-surface contact (SSC), kinematic coupling (KC), warping inclusive kinematic coupling (WIKC), discrete fasteners (DC).

6.4 Boundary condition

The boundary conditions during the earthquake loading are given in Figure 14. The base of the structure is entirely fixed except for the degree of translation in the x direction during the dynamic, where an acceleration signal corresponding to a real earthquake is introduced. The out-of-plane displacement above the beam-column joint is prevented in order to model the slab effect. The out-of-plane displacement and twist of the beams are prevented at $1.5 d_b$ of the column's face as required by AISC, 2016b and AISC, 2016c. The out-of-plane-displacement and vertical displacement are prevented at the symmetric axis of the original structure. Note that during the axial loading step, the vertical displacement is permitted so that the beam is not loaded. The leaning column out-of-plane and vertical displacement are fixed whereas the rotation and the x-translation are released. The acceleration real earthquake signal is also applied to the base of the leaning column. The leaning column's out-of-plane displacement is prevented on each floor. Note that the boundary condition shown on Figure 14 are unchanged throughout the upper floors. To be conservative, the support of the panel zone provided by the secondary beams is not modeled. Since the purpose of this report is to analyze the buckling of the panel zone, it is preferable to leave it free to move in the out-of-plane direction.

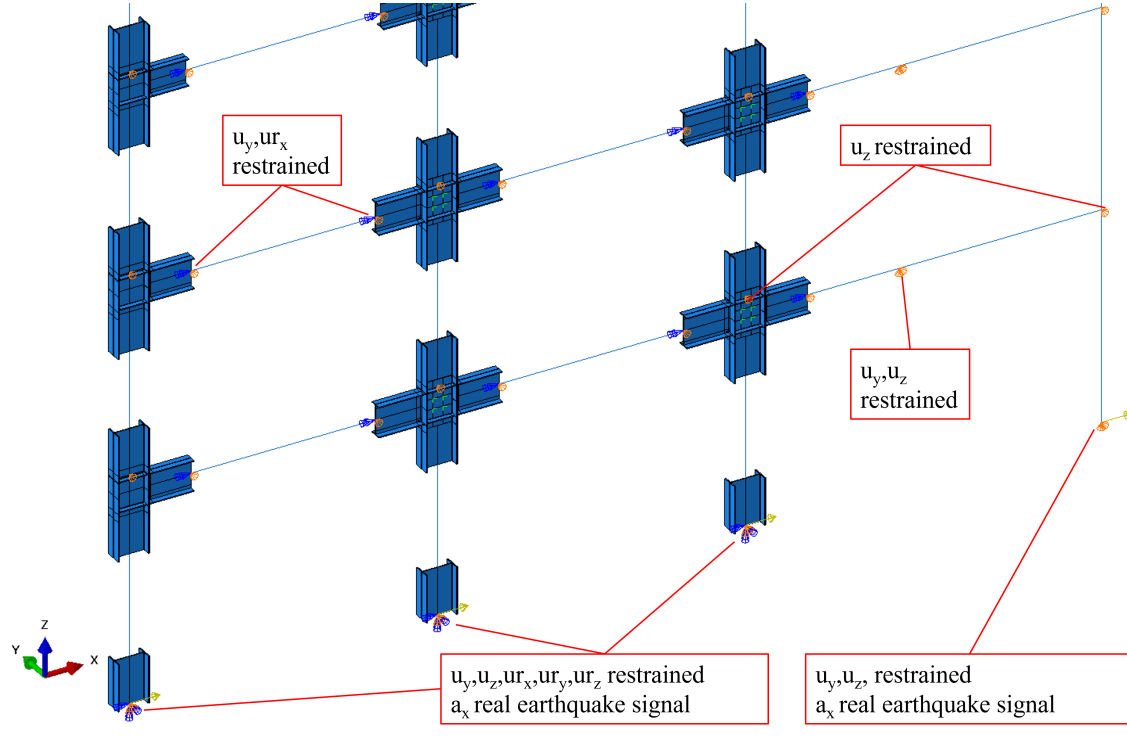


Figure 14: Boundary condition of the structure during the earthquake loading step.

6.5 Mass and loads

This section discusses the masses and loads considered in the building model. The mass and loads are computed in section 4.

The forces representing the actions in the building are concentrated forces. This simplified introduction of forces, compared with a distributed load on the beams, is due to the simplicity of the modeling, but also to the simplified static system of the structure (half-structure). Indeed, a load distributed on the beams at the level of the structure's axis of symmetry (beam span reduced by half) generates different forces in the original and reduced systems. Although this way of introducing force does not create a gravitational force in the beams, the effects of these actions represent a small contribution in the analysis situation under seismic load ($M_{Ed,G} \leq 0.09 \cdot M_y$).

In order to avoid stress concentration due to the introduction of point forces, the forces are introduced at reference points. These reference points are linked to a cross-section of the column using a rigid body constraint. The cross-section is located 20 mm above the upper beam flange (see Figure 12). Forces are introduced linearly in a static analysis step preceding dynamic analysis.

The concentrated masses (Figure 6) are introduced in the model using point mass inertia. This feature permits the input of a concentrated mass and a mass-proportional Rayleigh damping factor, α_R . The mass is attached to the reference point abovementioned in the previous paragraph. The density of the steel material is set to a small numerical value that does not correspond to the actual density. Due to the method of force computation for the post-processing stage of the result (see subsection 7.1.6), the damping and inertia forces of the structural element are negligible.

6.6 Strong panel zone design

In order to investigate the differences in behavior brought about by a design allowing greater inelastic deformation in the panel zone, a design with a strong panel zone is established. The panel zone is intended to remain elastic during the earthquake. As in conventional capacity design (AISC, 2016b), the panel zone

resistance must withstand the fully yielded and strained hardened resistance of the beams, M_{pl} , at the joint. The plastic resistance of the beams is as follows.

$$M_{pl} = \gamma_{ov} \cdot Z \cdot R_y \cdot f_y$$

With the overstrength factor, $\gamma_{ov} = 1.4$, and the plastic section modulus, Z , and the ratio of the expected yield stress to the specified minimum yield stress, R_y . The shear force acting on the interior panel zone is

$$V_{pz} = \frac{2M_{pl}}{(d - t_{bf})}$$

Conservatively we neglect the shear coming from the columns. A thickness of the doubler plate, $t_{dp} = 35 \text{ mm}$ is set so that the panel zone yield resistance, V_y , according to Skiadopoulos et al., 2021 is bigger than the panel zone shear, V_{pz} .

7 First story model validation

7.1 Push-over analysis

In this section, a push-over analysis is carried out on the second floor of the building described in section 6. This analysis is used to validate the consideration of element deformations and the calculation of forces acting on columns, beams, and panel zones. A displacement boundary condition is imposed at the head of each column, producing a maximum story drift of 5.6%.

7.1.1 Lateral stiffness derivation

The push-over analysis consists of lateral displacement boundary conditions on each column resulting in a total base shear force, F . The structure is divided into three subsystems that are composed of the following element,

- column below the inflection point
- column above the inflection point
- beams
- panel zone

The element stiffnesses in the subsystems are combined in series, and the subsystem stiffnesses are combined in parallel.

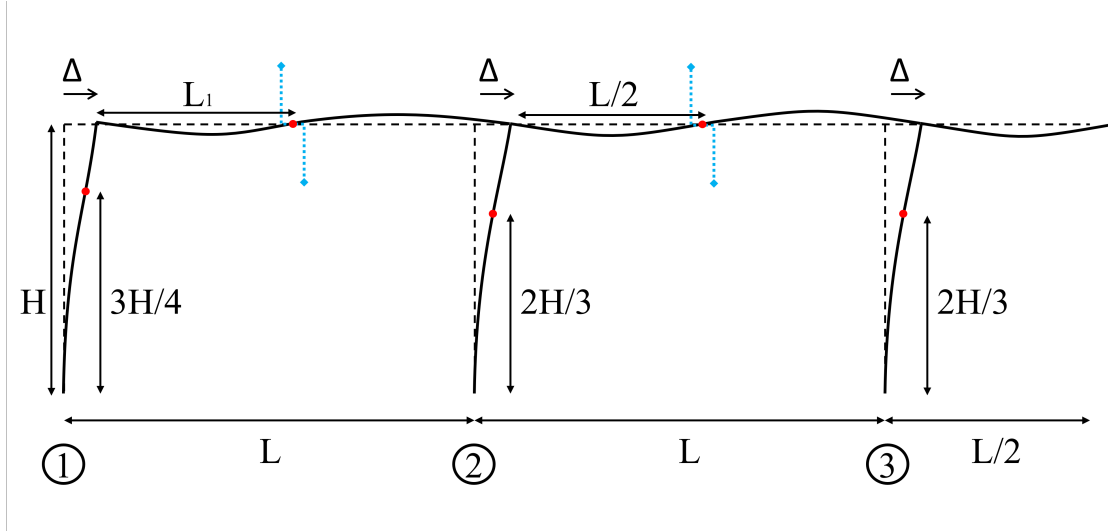


Figure 15: Story deformation. The inflection points are indicated with red dots. The columns are numbered from one to 3. The blue dashed lines represent the demarcation line of the sub-systems

However, as an initial guess, let's first assume that the inflection points in the columns are located at $3/4H$ and $2H/3$ from the base, in the exterior and the interior columns respectively. The lateral bending stiffness in the base column sub-assembly is given by

$$K_{c,base,1} = \frac{3EI_c}{(3H/4)^3}$$

$$K_{c,base,2} = K_{c,base,3} = \frac{3EI_c}{(2H/3)^3}$$

The lateral bending stiffness of the columns in the top sub-assembly is as follows

$$K_{c,top,1} = \frac{3EI_c}{(H/4)^3}$$

$$K_{c,top,2} = K_{c,top,3} = \frac{3EI_c}{(H/3)^3}$$

Combining the lateral stiffness in series for each column gives each column the total lateral bending stiffness.

$$K_{c,bending,1} = (1/K_{c,base,1} + 1/K_{c,top,1})^{-1}$$

$$K_{c,bending,2} = (1/K_{c,base,2} + 1/K_{c,top,2})^{-1}$$

We assume that the displacement at the top of each column should be equal, so the bending lateral stiffnesses are combined in parallel.

$$K_{c,bending,tot} = \sum_{i=1}^3 K_{c,bending,i}$$

Assuming that the columns are governing the lateral stiffness of the system compared to the panel zone and the beams, the column shear force, F_i , for each column, is given by

$$F_i = K_{c,bending,1}/K_{c,bending,tot} \cdot F$$

Knowing the shear force in each column, we can deduce the bending moment withstood by each column.

$$M_1 = F_1 \cdot H/4$$

$$M_2 = M_3 = F_2 \cdot H/3$$

Note that we assume that beam ends sharing the same joint endure the same bending moment. Assuming the moment to be linearly distributed in the beams, the inflection point can be deduced.

$$L_1 = \frac{M_1}{(M_1 + M_2)} \cdot L$$

$$L_2 = L_3 = L/2$$

Having defined all inflection points, three sub-systems are defined (Figure 15). The lateral bending stiffness of the beams is

$$K_{b,bending,1} = F/\delta_b = \frac{F}{M_1/(3EI_b/L_1) \cdot H/4}$$

$$K_{b,bending,2} = F/\delta_b = \frac{F}{M_2/(3EI_b/(L - L_1 + L_2)) \cdot H/3}$$

$$K_{b,bending,3} = F/\delta_b = \frac{F}{M_3/(3EI_b/L) \cdot H/3}$$

The shear stiffness for the columns is given by

$$K_{c,shear,i} = \frac{G \cdot A_v}{H}$$

$$A_v = (d - t_f) \cdot t_w$$

with A_v the effective shear area for the I-shape cross-section (Charney et al., 2005), d and t_f the depth and the thickness of the flanges. The total shear transmitted by the beams is equal to

$$\begin{aligned} V_{tot} &= V_1 + V_2 + V_3 \\ V_1 &= \frac{M_1 + M_2}{L} \\ V_2 = V_3 &= \frac{2M_2}{L} \end{aligned}$$

The beams' shear stiffness is found taking into account the transmitted shear.

$$K_{b,shear,i} = F/V_i \cdot \frac{G \cdot A_v}{L}$$

The panel zone stiffness, K_e , is computed using the model proposed in (Skiadopoulos et al., 2021). This model considers the bending and shear deformation of the panel zone.

$$\begin{aligned} K_e &= \frac{K_s \cdot K_b}{K_s + K_b} \\ K_s &= A_v \cdot G = (d_b - t_{bf}) \cdot t_{pz} \cdot G \\ K_b &= \frac{12EI}{d_b^3} \cdot d_b \end{aligned}$$

with the shear stiffness, K_s , and the bending stiffness, K_b . The panel zone thickness, t_{pz} , and the second moment of inertia, I , should take into account the presence of the doubler plate if any. The panel zone shear force is determined in the following way

$$\begin{aligned} V_{pz,1} &= \frac{M_1}{(d_b - t_{bf})} - F_1 \\ V_{pz,2} = V_{pz,3} &= \frac{2 \cdot M_2}{(d_b - t_{bf})} - F_2 \end{aligned}$$

The lateral displacement over the whole story is given by the formula from Skiadopoulos, 2022

$$\begin{aligned} \delta_{pz,1} &= \gamma_1 \left(1 - \frac{d_c/2}{L_1} - \frac{d_b/2}{H/4} \right) = \frac{V_{pz,1}}{K_{e,1}} \left(1 - \frac{d_c/2}{L_1} - \frac{d_b/2}{H/4} \right) \\ \delta_{pz,2} &= \gamma_2 \left(1 - \frac{d_c}{L - L_1 + L_2} - \frac{d_b/2}{H/3} \right) = \frac{V_{pz,2}}{K_{e,2}} \left(1 - \frac{d_c}{L - L_1 + L_2} - \frac{d_b/2}{H/3} \right) \\ \delta_{pz,3} &= \gamma_3 \left(1 - \frac{d_c}{L} - \frac{d_b/2}{H/3} \right) = \frac{V_{pz,3}}{K_{e,3}} \left(1 - \frac{d_c}{L} - \frac{d_b/2}{H/3} \right) \end{aligned}$$

Finally, the lateral stiffness of the panel zone is given

$$\begin{aligned} K_{pz,1} &= F/\delta_{pz,1} \\ K_{pz,2} &= F/\delta_{pz,2} \\ K_{pz,3} &= F/\delta_{pz,3} \end{aligned}$$

The lateral stiffness for each sub-system is found by the parallel combination of the stiffnesses.

$$K_{tot,i} = (1/K_{c,bending,i} + 1/K_{b,bending,i} + 1/K_{c,shear,i} + 1/K_{b,shear,i} + 1/K_{pz,i})^{-1}$$

The total lateral stiffness is the parallel combination of the lateral stiffness of the 3 sub-systems.

$$K_{tot} = \sum_{i=1}^3 K_{tot,i}$$

Finally, the shear force repartition in the column is refined using the total stiffness. The shear forces in the columns are computed and the whole procedure is done once again. Furthermore, the inflection point assumption is replaced with the actual inflection point location measured in the software. Figure 16 shows the total base shear versus the story drift ratio. The lateral stiffness developed above matches accurately the elastic stiffness of the simulation.

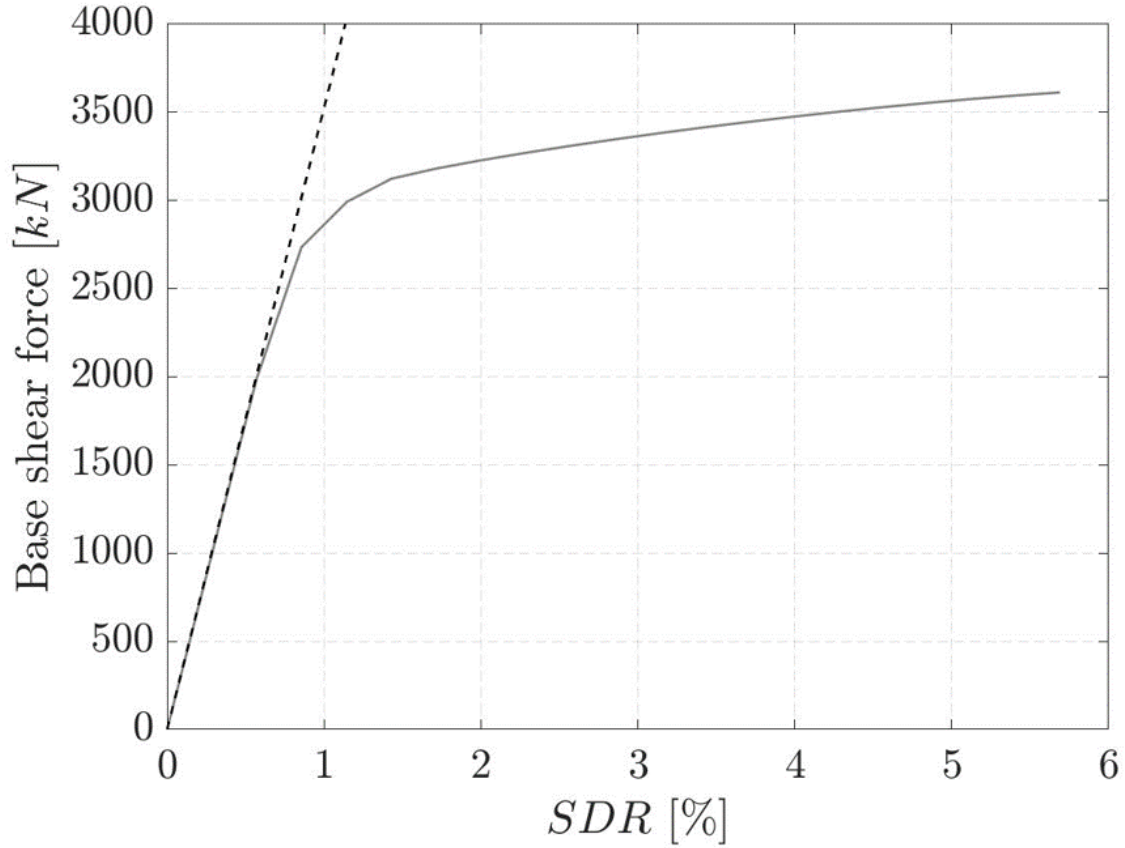


Figure 16: Lateral deformation of the structure versus the base shear. Computed elastic lateral stiffness represented with the dashed line

The reader will note that the deformation computation for a building with one or more stories will not be changed. In fact, the deformation of the second-story columns does not contribute to the displacement of the first story, as can be seen from the Figure 17. For this reason, the formulas developed above and in the next section are valid for buildings with more than one story.

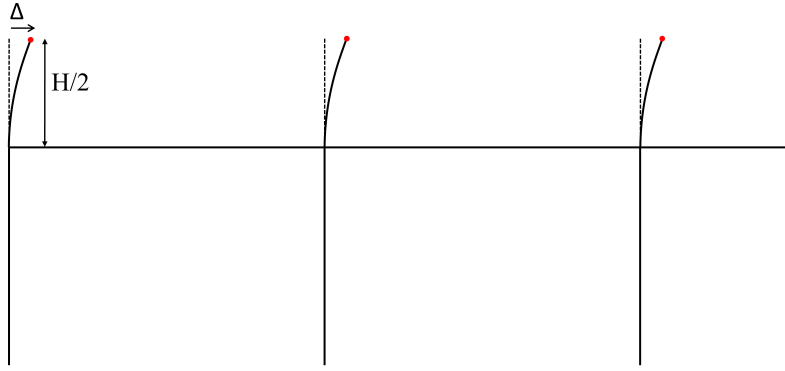


Figure 17: Lateral deformation due to columns of the second story, assuming that the rigid panel zone, beam, and first story columns are rigid.

7.1.2 Shear distortion

The coordinates of four points on the column web are recorded through the analysis. The measuring points are located on the column web in the corners of the panel zone. The shear distortion is obtained with the following formula from (Shin, 2017).

$$\gamma = \frac{\sqrt{a^2 + b^2}}{2ab} (\Delta_1 - \Delta_2)$$

where a and b are the horizontal and vertical distances between the measurement point in the undeformed geometry. δ_1 and δ_2 are the absolute displacements measured across the panel zone.

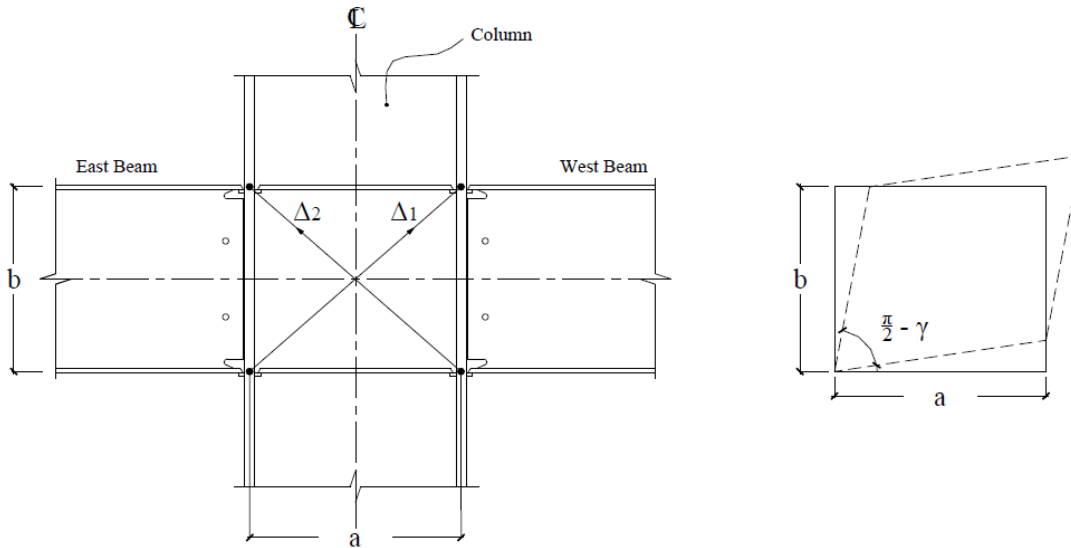


Figure 18: The measurement points are located on the column web and not on the flanges, as shown in the figure. Figure from Shin, 2017

The shear distortion, γ , can be decomposed into the column face rotation, θ_1 , and the column cross-section

rotation, θ_2 .

$$\gamma = \theta_1 + \theta_2$$

Then the following applies

$$\theta_2 \cdot d_c/2 = \theta_1 \cdot L_b$$

The column flanges rotation, θ_1 , and the rotation of the column cross-section, θ_2 are

$$\theta_1 = \gamma \cdot \frac{d_c}{2L_b + d_c}$$

$$\theta_2 = \gamma \cdot \frac{1}{1 + \frac{d_c}{2L_b}}$$

The story rotation due to the panel zone shear distortion, θ_{pz} is given by (Figure 19)

$$\theta_{pz} = \Delta_\gamma / (H_c + d_b/2) = (\theta_2 \cdot H_c - \theta_1 \cdot d_b/2) / (H_c + d_b/2)$$

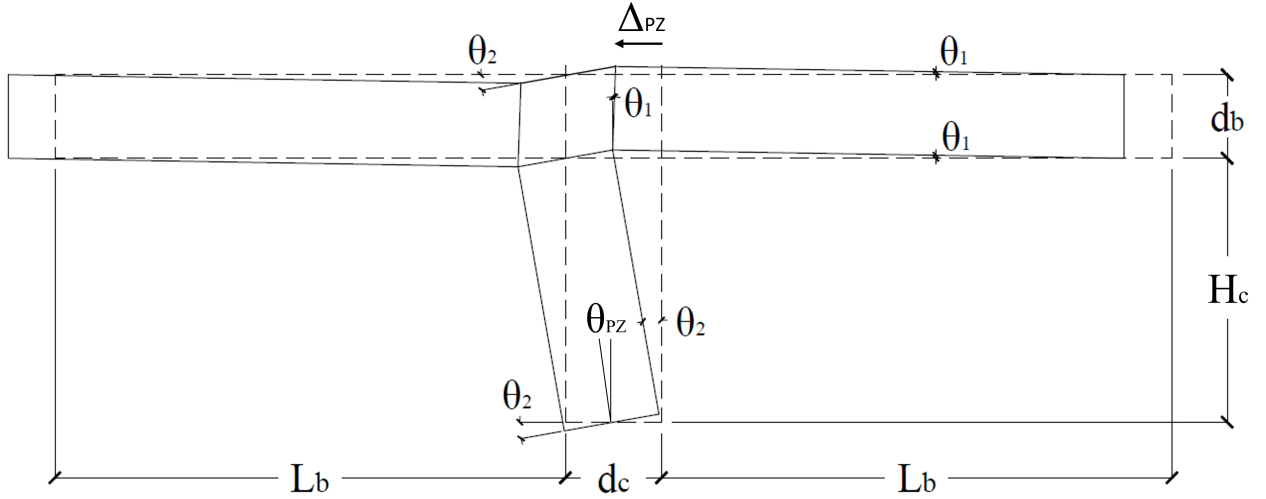


Figure 19: Story drift angle due to the panel shear distortion. Adapted from (Shin, 2017)

7.1.3 Beam chord rotation

As we are in a column-loaded configuration, the formula developed by Skiadopoulos, 2022 cannot be applied to retrieve the beam chord rotation. The story rotation due to deformation of the beams, θ_b , must be retrieved as follows (Shin, 2017)

$$\theta_b = \theta_{cf} - \theta_1$$

where θ_{cf} is the average rotation of the column flange computed with the coordinate of two points per column face at the top and bottom of the beam flanges. Then, the chord rotation of the beam θ'_b is linked to θ_b in the following manner

$$\theta'_b = \theta_b \frac{L_b + d_c/2}{L_b}$$

Figure 20 depicts the beam end moment compared to the chord rotation. The rotational elastic stiffness, $K_{beam,\theta}$, is computed considering a mid-span inflection point, and shear and bending deformations are included in the beam elastic stiffness.

$$K_{beam,\theta} = \left(\frac{L_i}{3EI} + \frac{1}{G \cdot A_v \cdot L_i} \right)^{-1}$$

Where L_i is the length of the inflection point for the beam of interest. The elastic stiffness is matching for the interior beam. Whereas for the exterior beams, the slight mismatch can be explained by the actual location of the beam inflection point. In fact, the inflection point is not located at mid-span but rather shifted to the right causing the exterior right end to be stiffer and the left end to be more flexible. The exterior beam is subjected to a greater axial load, this can explain the vertical shift between the exterior and the interior $M - \theta'_b$ curves.

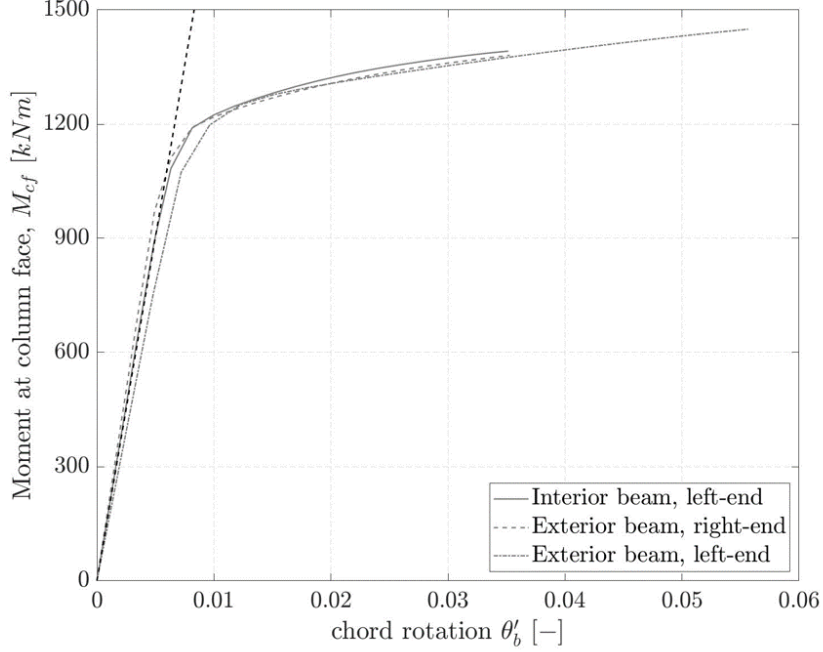


Figure 20: Beam end moment at the column face versus beam chord rotation, with beam elastic stiffness (black dashed line)

7.1.4 Top column chord rotation

First the story rotation due to the deformation of the columns θ_c is given by

$$\theta_c = SDR_{top} - \theta_b - \theta_{pz}$$

with the story drift ratio of the top sub-assembly, SDR_{top} , found using the lateral displacement at the inflection point location. Then, The column chord rotation is

$$\theta'_c = \theta_c \frac{H_c + d_b/2}{H_c}$$

The reader remarks that the top sub-assembly SDR_{top} can only be retrieved when the inflection point of the column is within the domain of the column length as the displacement must be extracted from the model.

7.1.5 Story drift validation

The chord rotation of the top columns is employed to control the deformation computation shown in the previous sections. The deformed angle between the chord of the column and the deformed cross-section, θ_m is measured in the software. Taking into account the rotation of the column cross-section, the measured story angle due to column rotation, $\theta_{c,m}$, is as follows

$$\theta_{c,m} = \pi/2 - (\theta_m - \theta_2)$$

This value can be compared to the value obtained in subsubsection 7.1.4. The relative error of the story rotation due to column deformation is

$$err_{\theta_c} = \frac{\theta_{c,m} - \theta_c}{\theta_{c,m}}$$

The error at the end of the push-over-analysis is equal to 1.9%.

7.1.6 Interior panel zone equilibrium

To verify the proper consideration of all moment and force components, this section will present the equilibrium of the interior panel zone. In order to avoid the tedious integration of stresses in the solid elements, forces and moments are recovered by the beam-column element. The element forces are given in the local coordinate system of the element, thus the deformed geometry has to be considered (Figure 21). At each element cut, the axial, N , shear forces, V , the strong axis bending moment, M , the tilt of the cut element, α , the vector to the panel zone center, OX and its inclination, β , are considered. The weak axis bending moment and shear, and torsion moment are neglected as their intensities are small and the rotation of the cross-section is small. The displacement boundary condition produces a reaction force, R_x .

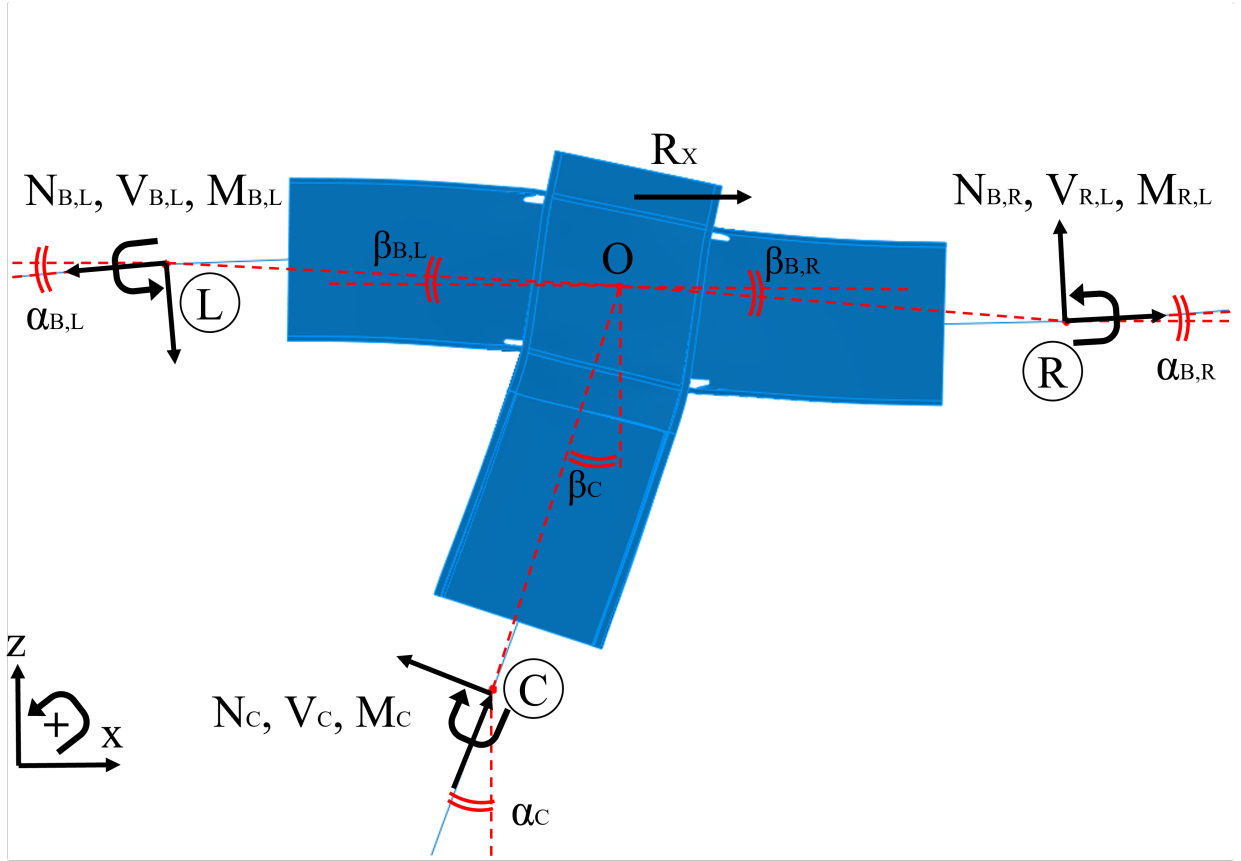


Figure 21: Force components and bending moments in the deformed geometry

Figure 22 shows the bending moment components at the panel zone center. The maximum bending moment equilibrium residual, $M_{eq,max} = 0.01 \text{ kNm}$, is negligible. The equilibrium of the vertical and horizontal forces has been done. However, as a matter of brevity, they are not shown in the report.

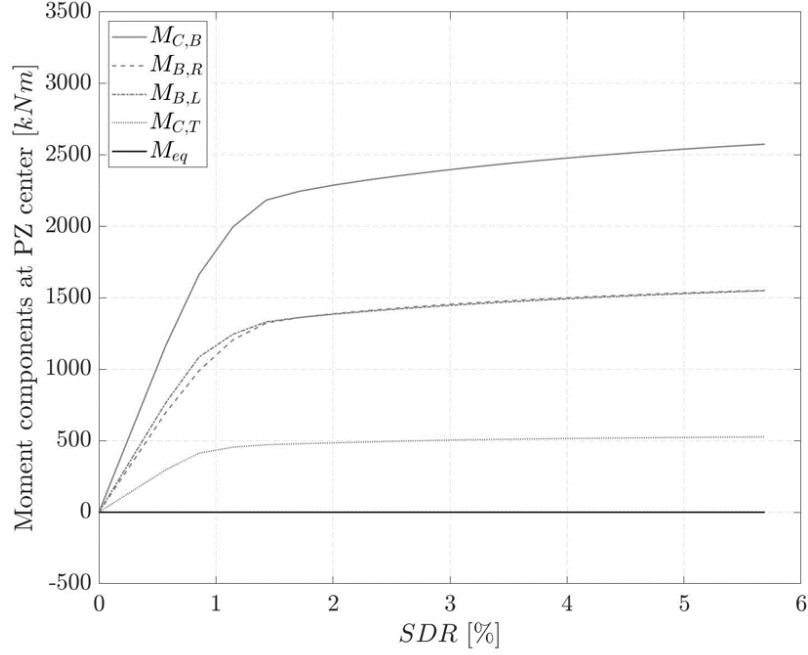


Figure 22: Bending moment components in absolute values at the panel zone center, and moment equilibrium residual.

7.1.7 Panel zone shear force

The simulation is compared to a panel zone shear resistance model (Skiadopoulos et al., 2021). This model is composed of 3 branches as conventional models (Krawinkler, 1978) employed in the design practice. The first branch depicts the elastic behavior, dominated by the shear stiffness of the web panel but it also takes into account the bending and shear stiffness of the flanges and the web panel in contrast with Krawinkler, 1978. The elastic stiffness of the panel zone is given by

$$K_e = \frac{V_{pz}}{\gamma} = \frac{K_s \cdot K_b}{K_s + K_b}$$

$$K_s = A_v \cdot G = t_{pz} \cdot (d_c - t_{cf}) \cdot G$$

$$K_b = \frac{12 \cdot E \cdot I}{d_b^3} \cdot d_b$$

The elastic stiffness of the column flanges, K_f is computed considering the shear and bending stiffness.

$$K_f = \frac{K_{sf} \cdot K_{bf}}{K_{sf} + K_{bf}}$$

$$K_{sf} = 2 \cdot (t_{cf} \cdot b_{cf} \cdot G)$$

$$K_{bf} = 2 \cdot \left[\frac{12E \left(b_{cf} \cdot t_{cf}^3 / 12 \right)}{d_b^3} \cdot d_b \right]$$

The panel zone yield force is

$$V_y = \frac{[0.58 (K_f / K_e) + 0.88] \cdot \frac{f_y}{\sqrt{3}} \cdot (d_c - t_{cf}) \cdot t_{pz}}{1 - K_f / K_e}$$

The post-yield behavior is described by two values of strength given at $4\gamma_y$ and $6\gamma_y$.

$$V_{pz} = \frac{f_y}{\sqrt{3}} \cdot [a_{w,eff} \cdot (d_c - t_{cf}) \cdot t_{pz} + a_{f,eff} \cdot (b_{cf} - t_{pz}) \cdot 2t_{cf}]$$

The flange participation factors are

$$a_{f,eff,4\gamma_y} = 0.93 (K_f/K_e) + 0.015$$

$$a_{f,eff,6\gamma_y} = 1.05 (K_f/K_e) + 0.02$$

The web participation factor are $a_{w,eff,4\gamma_y} = 1.1$, and $a_{w,eff,6\gamma_y} = 1.15$. Moreover, the strength reduction due to the axial gravity load is considered with the Von Mises criterion as suggested in Skiadopoulos et al., 2021. Moreover, the minimum axial force between the adjacent beams is also considered in the reduction. The axial force withstood by the column web compared to continuity plates is deduced from stiffness pro-rata repartition.

The shear force demand in the panel zone is computed according to Figure 23. The shear force on each panel zone face is computed in the deformed geometry.

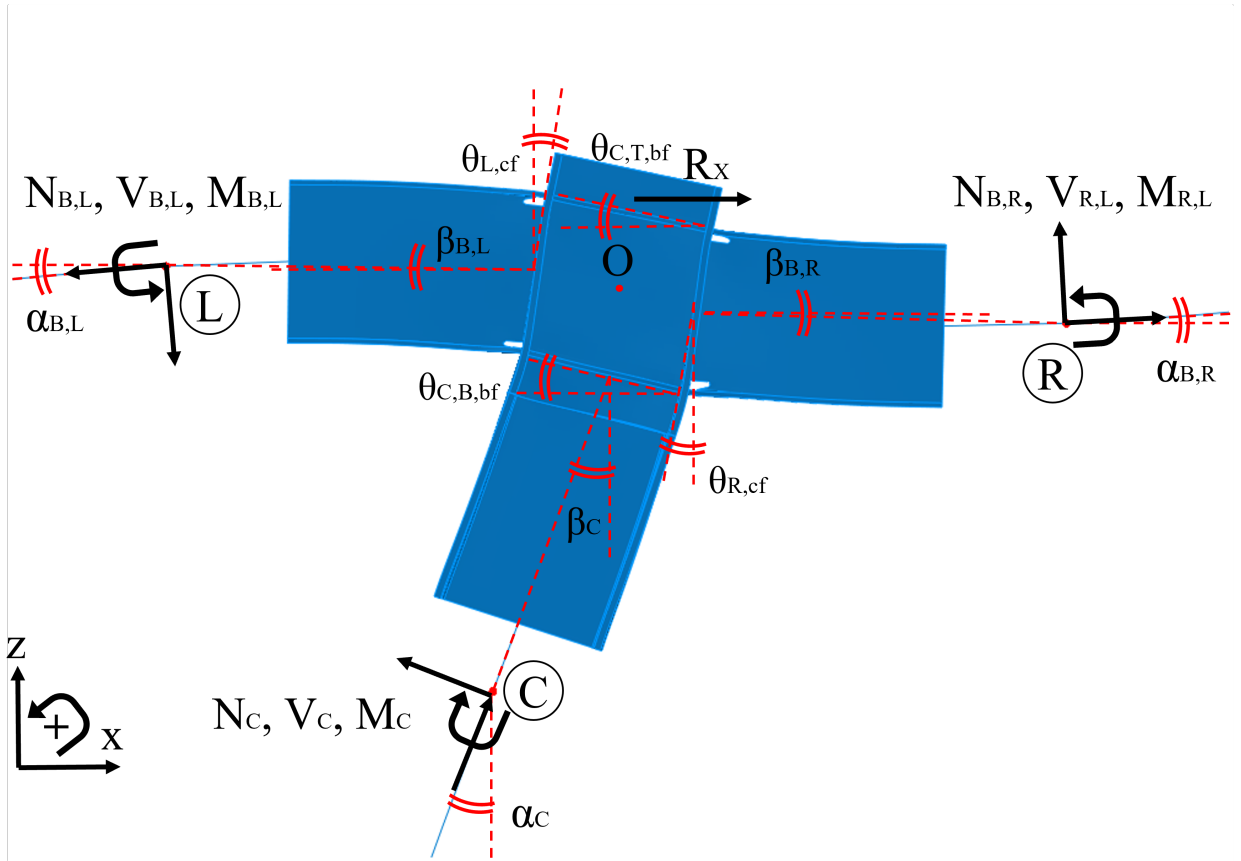


Figure 23: Shear force acting on the panel zone in the deformed geometry

As the axial force of the left and right sides are not in equilibrium, the shear coming from the top is not equal to the panel zone bottom shear. This means that the axial force differential of the beams induces a shear force on the panel zone. In fact, the shear stresses in the panel zone do not reach their maximum at the panel zone center, this maximum is rather shifted to the top of the panel zone ($N_{B,L} \geq N_{B,R}$).

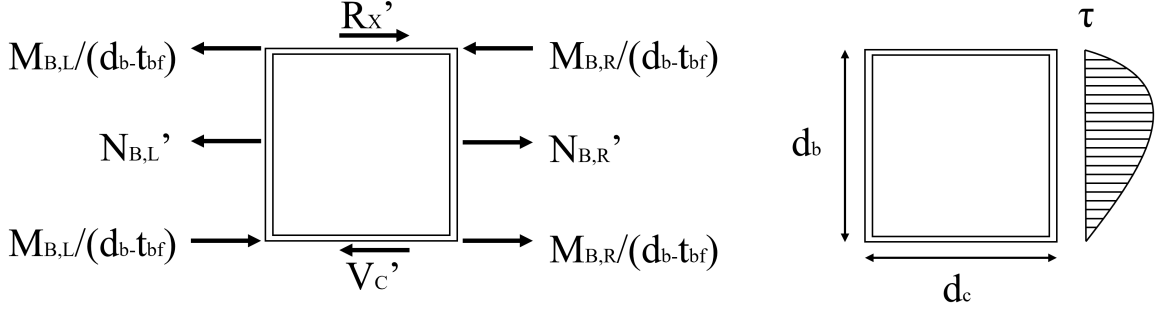


Figure 24: Force acting on the panel zone (left) and shear stresses distribution (right). Forces denoted with $'$, are computed in the deformed geometry

In order to take into account the worst-case demand for the panel area, the minimum shear force between the top and bottom columns is subtracted from the shear coming from the beams.

$$V_{pz} = \frac{M_{B,L} + M_{B,R}}{(d_b - t_{bf})} - \min(R_x', V_c')$$

Figure 25 shows the panel zone shear force versus the shear distortion for both the interior and exterior panel zone. Both panel zones are considered slender, $K_f/K_e \leq 0.02$. The exterior panel zone behaves according to Skiadopoulos et al., 2021. However, the limited amount of shear distortion does not permit the analysis of a large portion of inelastic behavior. The beam axial force applies a maximum 3% axial load ratio on the column web. The elastic panel zone stiffness is similar to the model's stiffness for both panels. Concerning the interior panel, the post-yield stiffness of the simulation is decreased by 66% compared to the model. Moreover, the strength difference is equal to 17% and 19% at $4\gamma/\gamma_y$ and $4\gamma/\gamma_y$ respectively. This substantial difference could be explained by the axial force in the beams. The panel zone strength model (Skiadopoulos et al., 2021) considers a pure shear state of the panel zone, whereas in the simulation an additional shear is added by the axial load differential in the beams. Research (El Jisr et al., 2020) on MRF with concrete slab, has shown the effect of beam axial load on the panel zone demand. Moreover, the difference could be due to the location of the recorded point employed to compute the shear distortion. Since these points are located on the web of the column, some of the shear distortion is not captured.

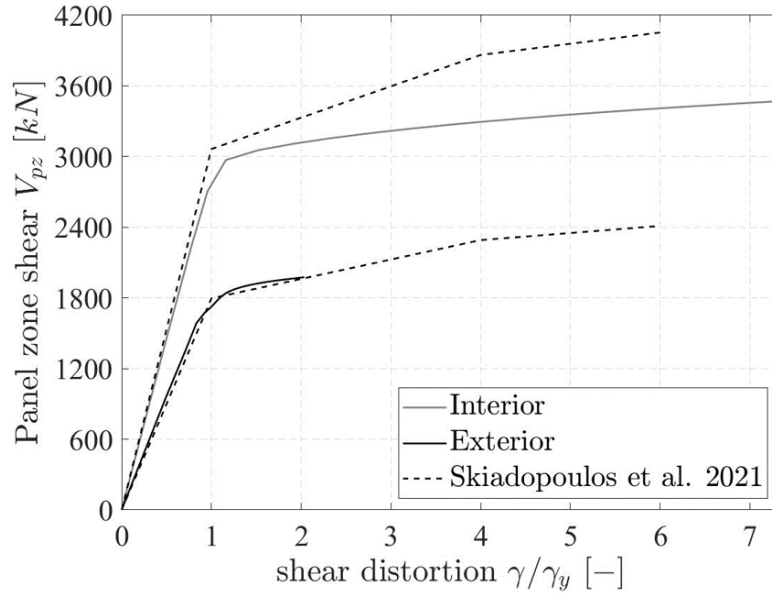


Figure 25: Panel zone shear force, V_{pz} versus shear distortion, γ

The axial load in the column due to the over-turning moment is shown in Figure 26. The exterior columns endure a large compressive axial force, whereas the interior columns have smaller tensile axial forces. The left interior columns' axial transient load is negligible.

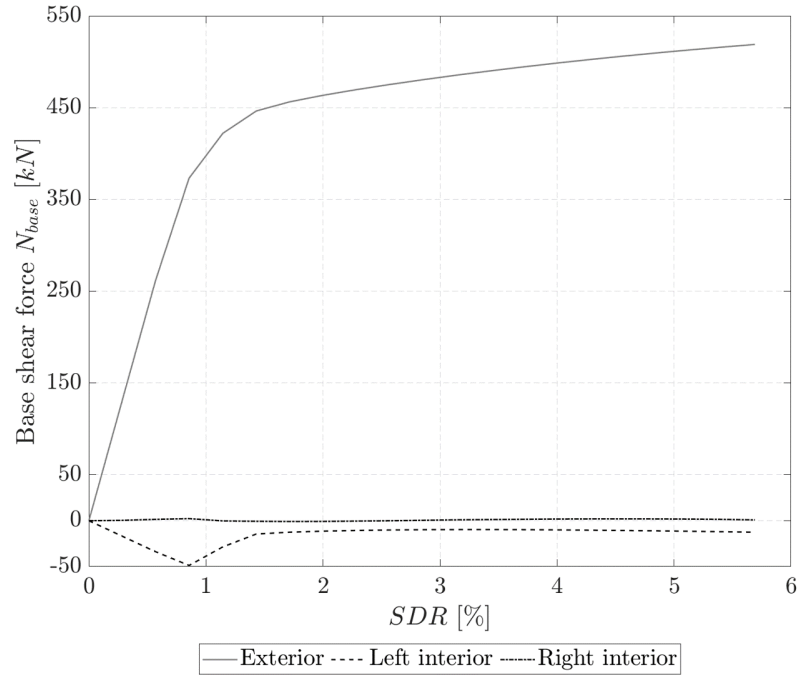


Figure 26: Axial force in the columns due to over-turning moment (no gravity loads applied)

7.2 Dynamic analysis

A dynamic analysis is conducted on the weak and strong panel zone design of the first story structure. In this section, three masses of 652.05 tonnes are inputted at the top of each column. A frequency analysis using Abaqus leads to a structural period of $T = 0.99s$ which is similar to the structural period deduced from the hand-calculated stiffness ($T = 0.96s$). A Rayleigh mass damping $\alpha_R = 0.628$, which corresponds to a damping ratio $\zeta = 4.95\%$, is inputted in the model. The scaled earthquake is considered (section 5). An axial load ratio of 20% is applied to the columns, and the axial load corresponding to the first story given in section 4 is applied to the leaning column.

The story drift ratio is shown in Figure 27. The peak story drift ratio, $SDR_{peak} = 3.68\%$, and 3.76% for the weak panel and strong panel designs respectively, is in the range of the elastic displacement given in section 5 ($SDR_{peak} = 2.6 - 9.0\%$). The peak permanent plastic deformation leads to a residual story drift, $SDR_{res} = 2.55\%$ for both designs. On the last 6 seconds of the signal (free oscillation), the damping ratio $\zeta = 2.5\%$, 1.9% , and the structural period, $T = 1.034s$ and $1.014s$ are computed for the weak and strong panel designs. The damping ratio and the period are retrieved by computing the logarithmic decrement and elapsed time over several oscillations. The structural period of the weak and the strong panel design $T = 1.014s$ are increased compared to their original value due to the yielding of the structure. Concerning the damping, the force created by the $P - \Delta$ effect acts on the system when it is oscillating. This means that the 6 last seconds of the signal are not free of all exterior forces. Thus, the damping ratio measured is very low compared to the input damping ratio (50%). To measure the damping ratio, some other means of computation should be employed to consider the $P - \Delta$ contribution. However, previous simulations with lower $P - \Delta$ effects have proven that the inputted damping ratio was on the order of 5%.

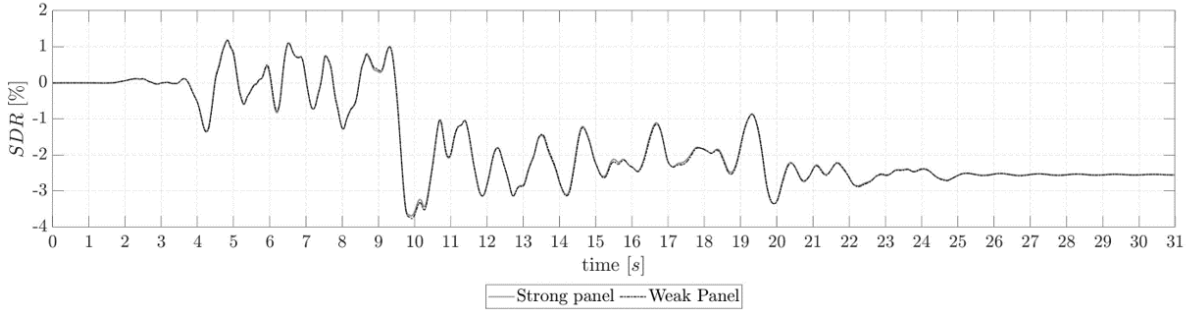


Figure 27: Story drift ratio versus signal time for the strong and weak panel zone design. Free oscillation starting from 25s.

Figure 28 shows the bending moment in the column and the beams and the residual equilibrium bending moment for the weak panel zone design. This residual is small compared to the moment involved in the equilibrium. The residual moment has a non-zero value at the end of the signal, suggesting that this residual can be attributed to permanent torsional and weak bending axis deformation.

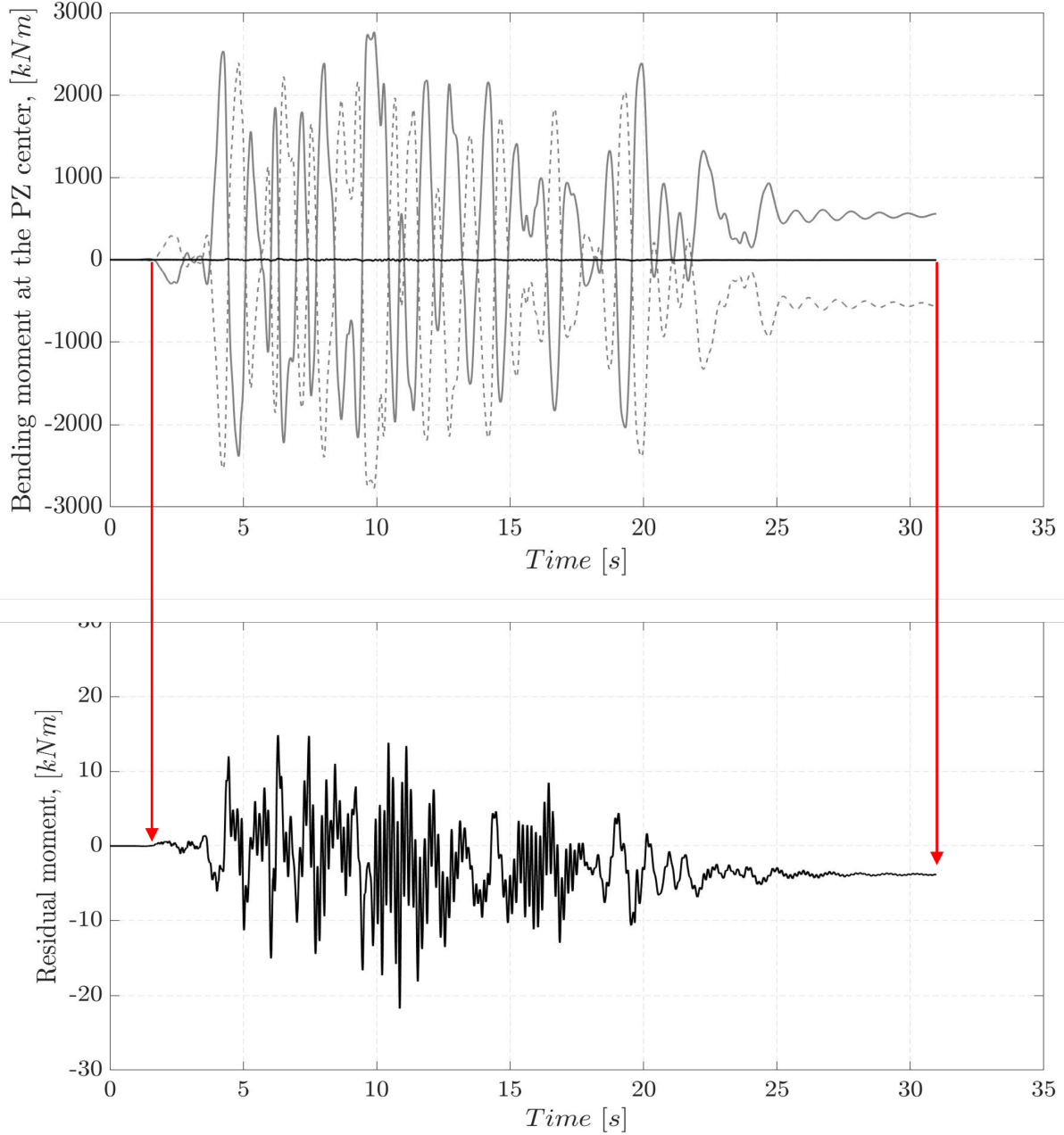


Figure 28: Bending moment at the panel zone center (top). The beam and column moment and residual moment are represented. A close-up look at the residual moment (bottom)

Figure 29 and Figure 30 depict the panel zone shear force and the shear distortion in the exterior and the interior joint respectively. The exterior panel behaves similarly in the weak and strong panel zone design. Limited inelastic shear distortion up to $1.5\gamma_y$ appears in the panel. The stiffness according to (Skiadopoulos et al., 2021) provides a satisfying estimation in dynamic analysis. The interior panel zone experiences inelastic distortion up to $5.6\gamma_y$ for the weak panel zone design. The simulation results sustain less force than the model prediction (see subsection 7.1.7). Considering the strong panel zone design, it seems that the measurements are perturbed. In fact, the interior column's top end is subjected to local buckling, thus twisting in the column gives false shear distortion values.

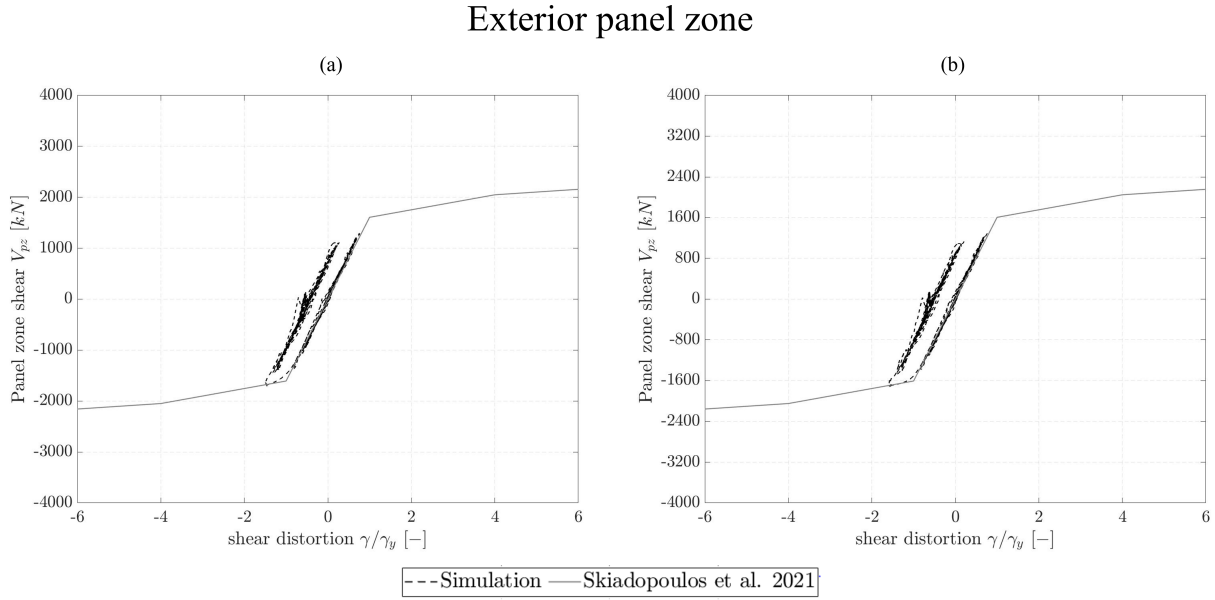


Figure 29: Shear force versus shear distortion in the panel zone for the exterior joint. Weak panel zone design (a), strong panel zone design (b)

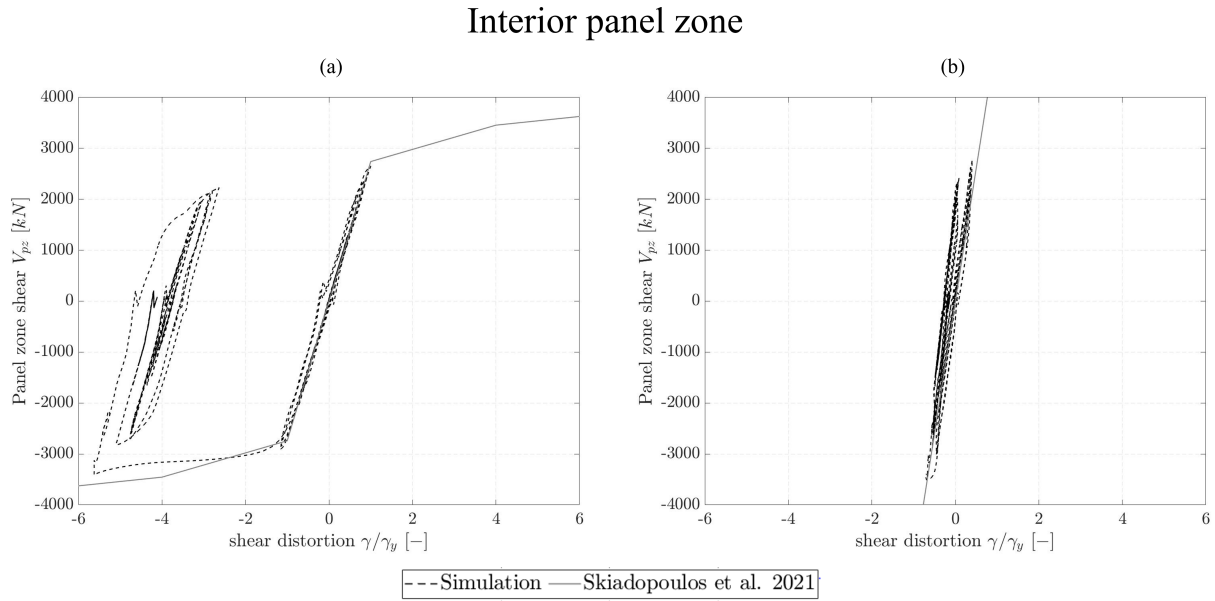


Figure 30: Shear force versus shear distortion in the panel zone for the exterior joint. Weak panel zone design (a), strong panel zone design (b)

The beam chord rotation and moment at the column face relation for both designs are shown for exterior beam Figure 31 and interior beam Figure 31. In general, the interior and exterior beams of the weak panel zone design have a uniform behavior. The beams do not experience lateral torsional buckling at their ends, although the stiffness of the exterior beam in the strong panel zone design is low at $\theta'_b = -0.035$. The demand for the interior beam in the strong PZ design is decreased compared to the exterior beam. The interior beam

shows limited inelastic behavior. In fact, the advantage of a weak panel zone design is to limit the demand on the beams to decrease the probability of lateral buckling of the beam ends. The reader notes that for some range in the column face bending moment data is missing. As described in subsubsection 7.1.3, when the structure regains its initial undeformed position, the inflection point tends to zero causing the beam chord rotation to tend to infinity. To dodge this issue, a minimal threshold inflection point length is set, $L_{b,min} = 4.0 \cdot d_c$.

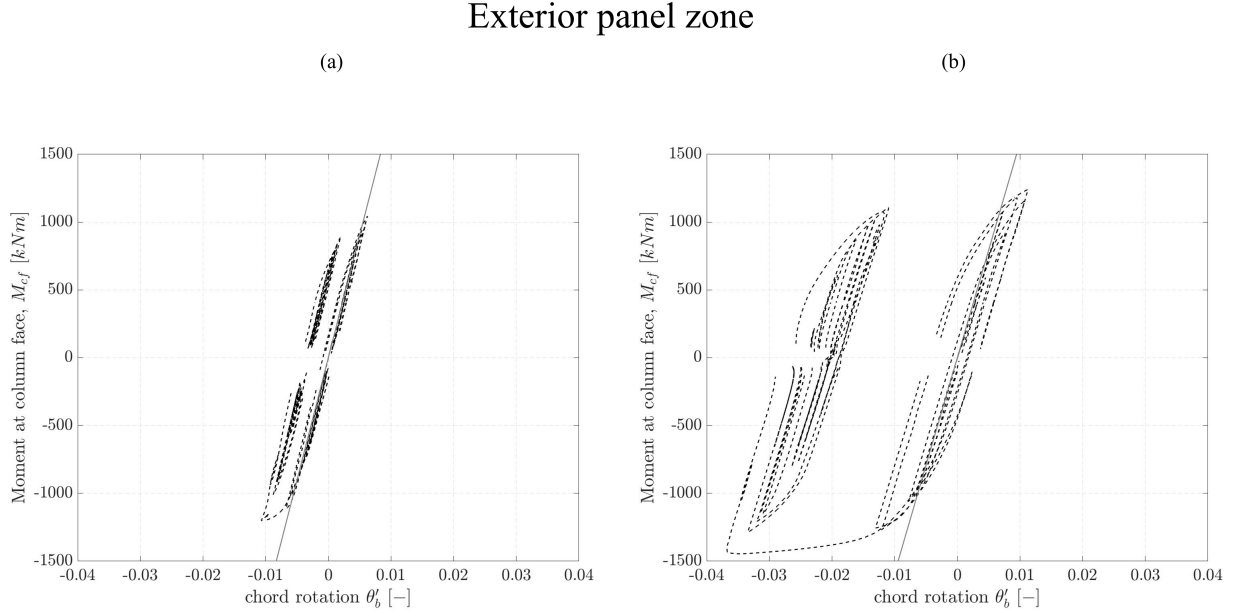


Figure 31: Moment at the column face for the exterior left-end beam. Weak panel zone design (a), strong panel zone design (b). Computed elastic stiffness (gray line)

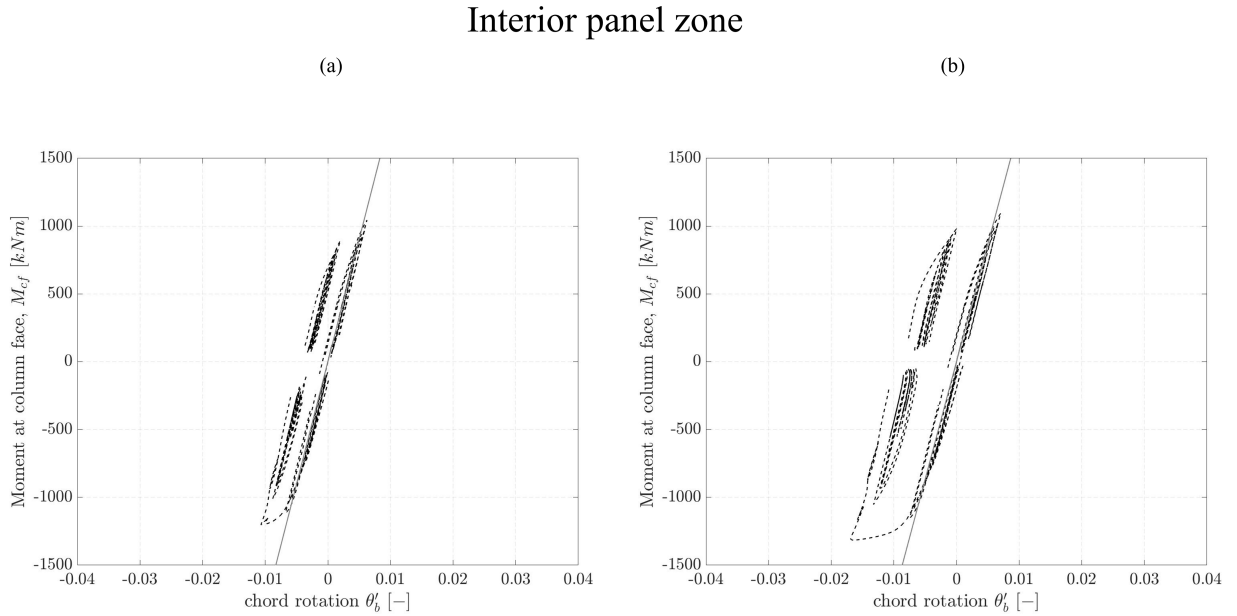


Figure 32: Moment at the column face for the interior left-end beam. Computed elastic stiffness (gray line)

The top column chord rotation versus the moment at the beam face is not represented. This is because an important amount of data is missing to get a meaningful chord rotation plot (column inflection point is not located on the column domain). However, local flexural buckling has been observed on the structure's interior left-hand column (Figure 33). The weak panel zone design does not show instabilities in this location. This type of instability in the column is not surprising. Indeed, as the building was designed on the basis of a column belonging to the upper floor, in the current situation the resistance of the columns in the joint is reduced. The SCWB ratio is therefore no longer respected, and the column is the fuse element.

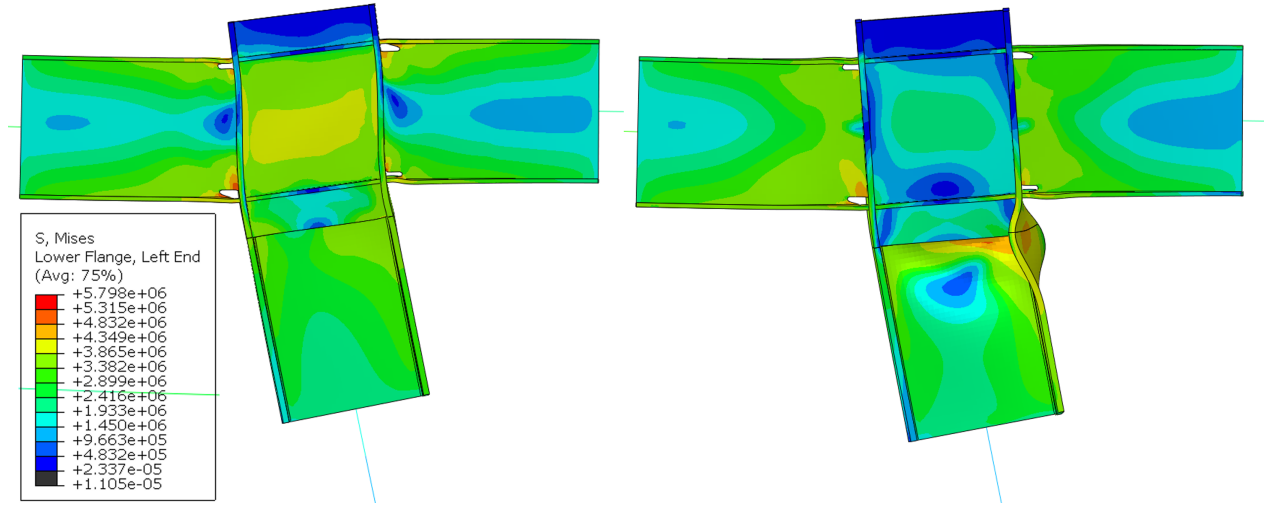


Figure 33: Weak (left) and strong (right) panel zone design at 8.6 seconds. The von-mises stress (N/dm^2) is shown on the deformed geometry (5 times scaled).

The base moment story-drift ratio shows some instability phenomenon, as the stiffness is negatively defined for $SDR = -1.75\%$ (Figure 34). The deformed structure shows high inelastic deformation localized at the column base ends. The reader notes that instabilities are initiated for a negative story drift ratio when the columns sustain the compressive axial force. In the same way, the bending moment capacity is greater for positive SDR values. Whereas in the case the full structure was modeled, this asymmetric behavior would not be noticed. The exterior column is more axially loaded, thus its moment capacity is decreased.

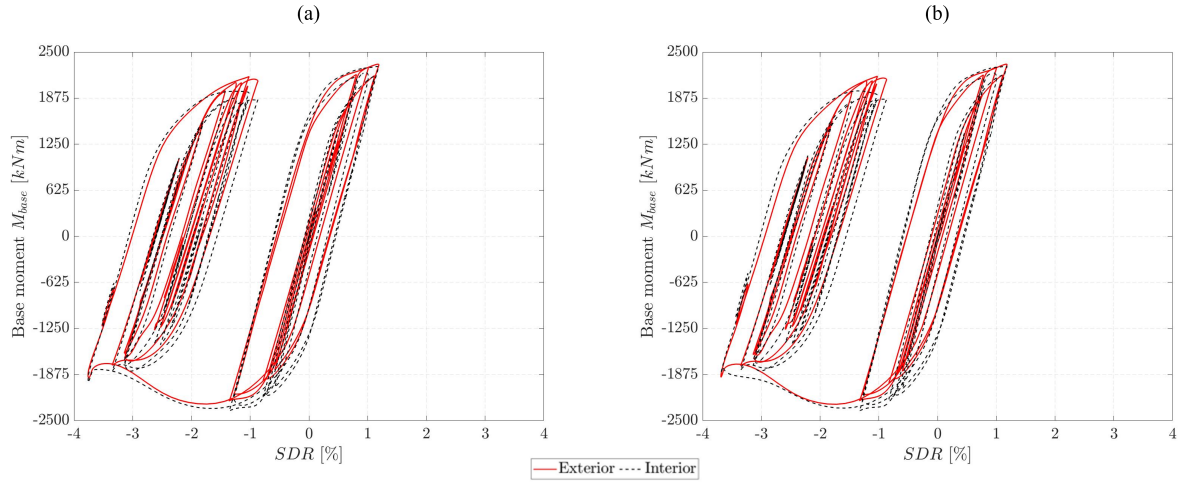


Figure 34: Base moment for the exterior and interior column for the weak (a) and strong design (b).

8 Eight story building results

8.1 Frequency analysis

Frequency analysis is carried out using Abaqus. The first structural period, $T_1 = 2.12$, found by Skiadopoulos, 2022 is slightly lower than the period found in the frequency analysis Table 5. The consideration of real cross-section dimensions and explicit modelization of the panel zone can explain that difference. The shape of the first three oscillation modes are depicted in Figure 35.

Mode number	-	1	2	3	4	5	8	9	10
EM/M_{tot}	%	78.17	12.04	4.69	2.48	0.01	0.00	0.82	0.37
Period T	s	2.27	0.78	0.44	0.29	0.23	0.18	0.16	0.13
ζ	%	5.96	2.05	1.15	0.76	0.59	0.48	0.42	0.34

Table 5: Frequency analysis results. EM/M_{tot} represents the effective modal mass in the translational direction compared to the total mass. The damping ratio, ζ_i found for each mode

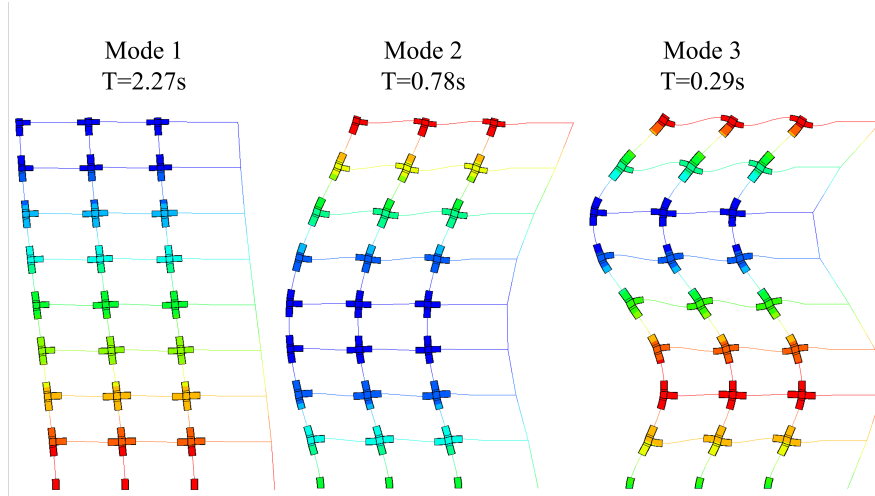


Figure 35: Deformed shape of the first three modes. The color plot represents the lateral displacement of the nodes (blue and red colors, corresponding to left and right displacement). The leaning column is represented on the right side of the structure.

The employed user-defined material employed (Hartloper et al., 2021) in the simulation does not permit the input of mass and stiffness Rayleigh damping. The mass damping coefficient, α_R , is added to the lumped mass of each column.

$$\alpha_R = 2\omega_i \cdot \zeta_i$$

where ω_i , and ζ_i are the structural pulsation and the damping ratio of mode i respectively. The mass damping coefficient is determined in order to have an average damping ratio, $\zeta_{avg} = 0.05$, in proportion to the mass contribution of the 10 first modes.

$$\zeta_{avg} = \frac{\sum_{i=0}^{10} EM_i \cdot 2 \cdot \alpha_R / \omega_i}{\sum_{i=0}^{10} EM_i}$$

The modes considered for the mass damping coefficient represent 94% of the effective mass. The average damping ratio causes the first mode to be overdamped $\zeta_1 > 5\%$.

8.2 Dynamic analysis

The analysis is carried out with the original earthquake signal. Unfortunately, some convergence problems cause the simulation to stop at 7.9 s. Those problems appear in the panel zone region of the first story. Looking at the iteration computation, the out-of-plane degree of freedom force residual is too large for nodes on the doubler plate. This means that the convergence problem is associated with the contact between the column web and the doubler plate. Several modifications were made to the original model in order to improve the results. First, an initial gap was created between the doubler plate and the column web to prevent friction contact to perturb the computation. Second, an attempt to tie the doubler plate to the column web was made. However, this could not be done because it created an overconstraints problem in the panel zone. Due to the model definition, it would have been too long to redefine a new model. The building remains in an elastic behavior for 7.9 seconds, although the analysis of the structural response is not able to provide remarks about the inelastic behavior of the structure, the analysis of the elastic behavior is carried out.

The peak story drift ratio, $SDR_{peak} = 0.91\%$, appears at the 4th story. The distribution of peak SDR is uniformly distributed in the range of 0.53% to 0.91%, over the height of the building (Figure 36 (a)). The distribution of the story shear over the height of the building depicts the phenomenon of higher oscillation mode (Figure 36 (b)).

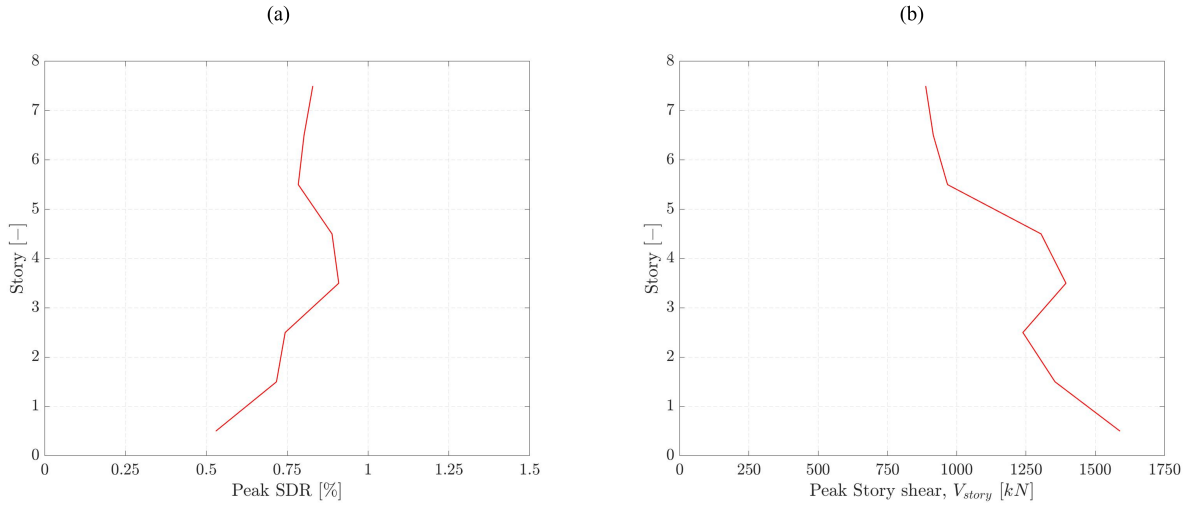


Figure 36: Peak story drift ratio (a) and peak story shear (b)

The panel zone response is shown in the Figure 37. The presence of higher mode amplification is seen on mid-height stories, as the peak shear distortion, $\gamma_{peak}/\gamma_y = 0.9$ appears at the 4th story.

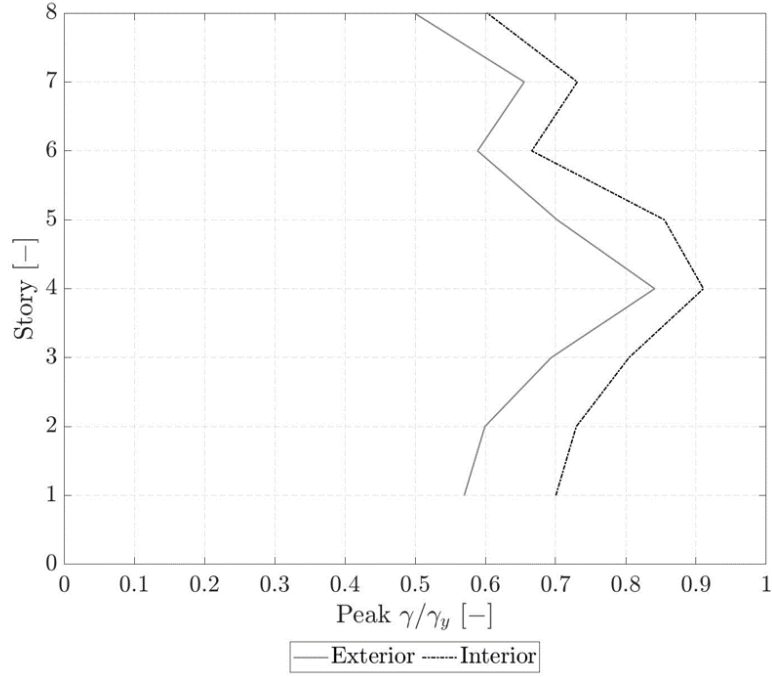


Figure 37: Peak shear distortion for exterior and interior panel zones.

The panel zone shear force of the 4th story is depicted in Figure 38. (Skiadopoulos et al., 2021) panel zone model better describes the elastic stiffness of the panel zone than the model from AISC, 2016c. The axial load ratio is accounted for in the panel zone shear strength models. Inertia effects can be seen in the response, as some panel zone shear force values are out of the elastic stiffness line.

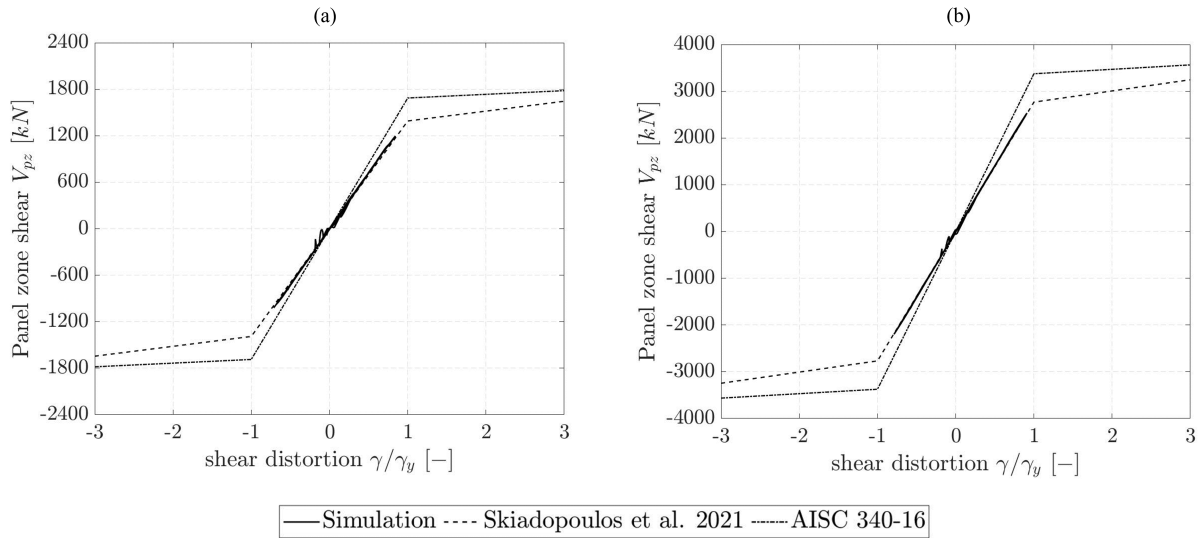


Figure 38: Shear force versus shear distortion for the 4th story exterior (a) and (b) panel zones. Panel zone shear resistance model according to Skiadopoulos et al., 2021 and AISC, 2016b.

The first story beams behave elastically (Figure 39). The elastic stiffnesses shown on the graph assume average locations over the response of the inflection points for the left-end exterior beam and a mid-span inflection point for the beams of the interior joint. The variation of the inflection point location is due to inertia effects and small asymmetries in the structure lateral response. The simulation results correspond relatively well to the elastic stiffness, 2.5%, 3.6%, and 3.1% stiffness relative difference to the simulation results for respectively the interior left-end, right-end, and interior left-end. The difference can be explained by the simplified hypothesis used for the elastic stiffness computation. Notably, the implementation of the shear stiffness for the beam elements does not correspond exactly to the one considered in the solid element part.

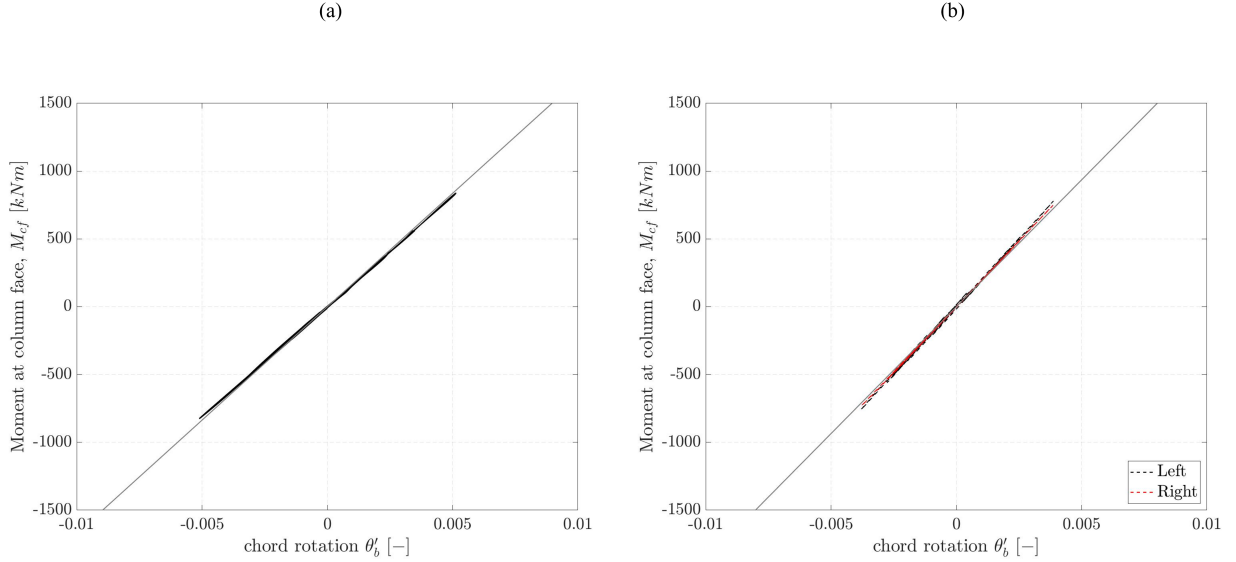


Figure 39: Bending moment at the column face of the exterior (a) and interior (b) panel zones. The interior panel zone has two faces, namely left and right.

The base moment of the column remains elastic. The simulation of the interior column is stiffer than the exterior column. The global moment created by the vertical eccentricity of the inertia forces in relation to ground level induces transient axial forces in the columns. Figure 40 (b) shows the axial forces absorbed by the outer and inner left-hand columns. The outer column absorbs a variable axial load of greater amplitude than the inner left column. This is due to a greater horizontal eccentricity in relation to the structure's axis of symmetry.

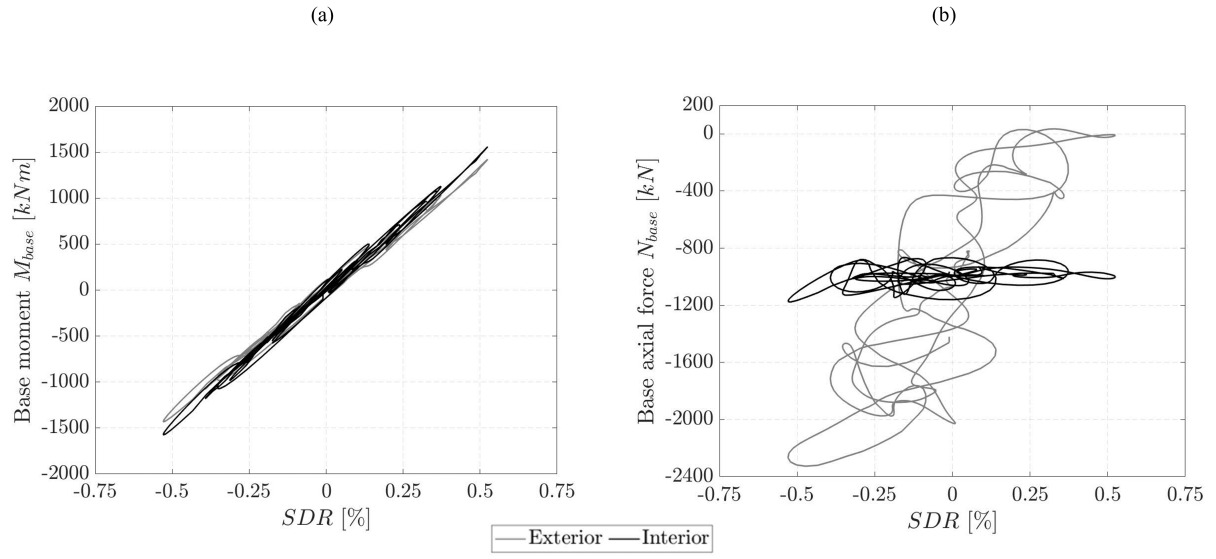


Figure 40: Base bending moment versus story drift ratio of the first story (a), and axial force of the first story exterior column and the left interior columns.

9 Conclusion

The objective of this study was to assess the stability of a steel moment-resisting frame (MRF) featuring high panel zone shear distortion design demand ($\gamma_d = 10\gamma_y$) subjected to a real earthquake ground motion.

Firstly, to investigate a building prone to shear buckling issues in the panel zone, an archetype building was selected based on previous research (section 12). The entire building and a substructure comprised of the first story only, were accurately modeled. A real earthquake ground motion acceleration signal was selected.

Then, the method employed to compute the beam chord rotation and panel zone shear were developed. In parallel, the force determination method was derived and validated through static push-over and dynamic analyses on the single-story structure. The elasto-plastic non-linear simulation results provided coherent behavior when compared to their analytical elastic counterpart. The behavior of the panel zone was studied, and the simulation results aligned well with the stiffness of the Skiadopoulos et al., 2021 model. However, discrepancies emerged in the post-yield range, likely due to the more complex stress state considered in the simulation and the location of shear distortion measurement points. The panel zone model proposed by Skiadopoulos et al., 2021 exhibited a better description of the panel zone elastic stiffness compared to the model commonly used in engineering practice (Krawinkler, 1978). The analysis of two structural designs, namely a weak and a strong panel zone design demonstrated the advantages of the former. The overall response of the first story was similar in both cases, but a higher proportion of inelastic deformation in the panel zone reduced the demand on columns and beams. No buckling occurred in the panel zone up to shear distortions of $5.6\gamma_y$ for the weak panel zone design, whereas flexural buckling occurred at the top of the columns in the strong panel zone design. It would have been interesting to further-push the weak panel zone design to high shear distortion to provoke the apparition of shear buckling.

Overall, this master thesis on the seismic analysis of an eight-story building with a weak panel zone design and the use of numerical simulations provides valuable insights into the system-level behavior associated with this design. However, due to time limitations, the full-building model could not fully capture the earthquake signal, and convergence issues need to be addressed. Modifying solver parameters or model parameters could potentially resolve these convergence issues. Multiple trial were made, however the computational time of the full building being long, the model modification could only be done few times. Despite the convergence issues, this project helped to model an eight story building and developed methods to extract data of interest from the simulation results.

It is important to note that the proposed building model does not consider the influence of composite action on panel zone behavior (El Jisr et al., 2020). This aspect should be taken into account in future studies. Additionally, the static system exhibited asymmetrical behavior due to the modeling of only half of the structure, which could lead to smaller instability issues compared to the overall behavior of the full structure.

10 Acknowledgment

I would like to acknowledge the following individuals for their invaluable contributions to the completion of my master thesis:

I extend my heartfelt appreciation to Tianyu for his expertise and support during the modeling phase on Abaqus, as well as his invaluable assistance in running the simulations. His dedication and guidance were crucial in obtaining accurate and reliable results.

I would also like to express my sincere gratitude to Ce for his assistance in addressing multiple questions that arose during my research. His willingness to share his knowledge and insights greatly enhanced the depth and clarity of my work.

I am deeply grateful to Andy for his invaluable help in validating the deformation decomposition. His meticulous attention to detail and insightful feedback played a pivotal role in ensuring the accuracy and reliability of my findings.

Finally, I would like to express my profound appreciation to Professor Lignos for his unwavering support throughout the semester and for providing me with the opportunity to explore such an intriguing research topic. His mentorship, guidance, and invaluable input significantly influenced the direction and quality of my thesis.

I am truly fortunate to have had the privilege of working with such exceptional individuals who have enriched my academic journey. Their expertise, patience, and willingness to assist have been instrumental in bringing this thesis to fruition.

I extend my heartfelt gratitude to each of them for their remarkable contributions, without which this achievement would not have been possible.

11 Data availability

All the models developed for this thesis, including the associated files, have been made available on the ENAC share. This ensures that the research and methodology can be reproduced and further explored by interested parties.

Moreover, I have made all the abaqus output database (ODB) files produced in the simulations accessible for reference, these are located on the Resslabserver2. These files contain the essential data necessary to analyze and validate the results obtained during the research process.

In addition, I have provided access to all the processed data, which includes the datasets derived from the simulations and experimental measurements. These datasets have been carefully organized and documented to facilitate further analysis and comparison.

To facilitate post-processing and data analysis, the MATLAB files used for processing the data have also been made available. These files contain the necessary algorithms and codes employed to extract and analyze the relevant parameters.

By ensuring the availability of the models, ODB files, processed data, and MATLAB files, I aim to promote transparency, reproducibility, and collaboration in scientific research. Interested individuals can access these resources on the ENAC share and utilize them for further investigations or to build upon the findings presented in this thesis.

References

- AISC. (2016b). *Seismic provisions for structural steel buildings, ANSI/AISC 341-16*. <https://www.aisc.org/globalassets/aisc/publications/standards/seismic-provisions-for-structural-steel-buildings-ansi-aisc-341-16.pdf>
- AISC. (2016c). *Specification for structural steel buildings, ANSI/AISC 360-16*. <https://www.aisc.org/globalassets/aisc/publications/standards/a360-16-spec-and-commentary.pdf>
- AWS, (W. S. (2016). *Structural welding code-seismic suplement. AWS D1.8/D1.8M:2016*.
- Blume, J. A. (1961). Design of multistory reinforced concrete buildings for earthquake motions.
- Charney, F. A., Iyer, H., & Spears, P. W. (2005). Computation of major axis shear deformations in wide flange steel girders and columns. *Journal of Constructional Steel Research*, 61(11), 1525–1558. <https://doi.org/10.1016/j.jcsr.2005.04.002>
- COSMOS: Northridge 1994-01-17 12:30:55 UTC. (n.d.). Retrieved June 27, 2023, from <https://www.strongmotioncenter.org/vdc/scripts/event.plx?evt=21>
- El Jisr, H., Elkady, A., & Lignos, D. G. (2020). Hysteretic Behavior of Moment-Resisting Frames Considering Slab Restraint and Framing Action. *Journal of Structural Engineering*, 146(8), 04020145. [https://doi.org/10.1061/\(ASCE\)ST.1943-541X.0002696](https://doi.org/10.1061/(ASCE)ST.1943-541X.0002696)
- Fardis, M. N. (2018). Capacity design: Early history. *Earthquake Engineering & Structural Dynamics*, 47(14), 2887–2896. <https://doi.org/10.1002/eqe.3110>
- Fielding, D. J., & Huang, J. S. (1971). Shear in steel beam-to-column connections. *Welding Journal*, 50(7), 313–326.
- Hartloper, A. R., de Castro e Sousa, A., & Lignos, D. G. (2021). Constitutive Modeling of Structural Steels: Nonlinear Isotropic/Kinematic Hardening Material Model and Its Calibration. *Journal of Structural Engineering*, 147(4), 04021031. [https://doi.org/10.1061/\(ASCE\)ST.1943-541X.0002964](https://doi.org/10.1061/(ASCE)ST.1943-541X.0002964)
- Hartloper, A. R., de Castro e Sousa, A., & Lignos, D. G. (2022). Warping-Inclusive Kinematic Coupling in Mixed-Dimension Macro Models for Steel Wide Flange Beam Columns. *Journal of Structural Engineering*, 148(2), 04021253. [https://doi.org/10.1061/\(ASCE\)ST.1943-541X.0003211](https://doi.org/10.1061/(ASCE)ST.1943-541X.0003211)
- Hartloper, A. R. (2021). *Reduced-order Models for Simulating Coupled Geometric Instabilities in Steel Beam-columns Under Inelastic Cyclic Straining*. EPFL. Lausanne. <https://doi.org/10.5075/epfl-thesis-8504>
- Islam, A., & Imanpour, A. (2023). Seismic stability of steel wide-flange columns in ductile moment-resisting frames: Out-of-plane response and design recommendations. *Bulletin of Earthquake Engineering*. <https://doi.org/10.1007/s10518-023-01653-7>
- Kim, K. D., & Engelhardt, M. D. (2002). Monotonic and cyclic loading models for panel zones in steel moment frames. *Journal of Constructional Steel Research*, 58(5), 605–635. [https://doi.org/10.1016/S0143-974X\(01\)00079-7](https://doi.org/10.1016/S0143-974X(01)00079-7)
- Krawinkler, H. (1978). Shear in beam-column joints in seismic design of steel frames. *Engineering Journal*, 15(3).
- Lee, D., Cotton, S. C., Hajjar, J. F., Dexter, R. J., Ye, Y., & Ojard, S. D. (2005). Cyclic behavior of steel moment-resisting connections reinforced by alternative column stiffener details I. Connection performance and continuity plate detailing. *ENGINEERING JOURNAL-AMERICAN INSTITUTE OF STEEL CONSTRUCTION*, 42(4), 189.
- Medhekar, M. S., & Kennedy, D. J. L. (2000). Displacement-based seismic design of buildings—theory. *Engineering Structures*, 22(3), 201–209. [https://doi.org/10.1016/S0141-0296\(98\)00092-3](https://doi.org/10.1016/S0141-0296(98)00092-3)
- Park, R., & Paulay, T. (1991). *Reinforced concrete structures*. John Wiley & Sons.
- Paul Popov, E., Yang, T.-S., & Chang, S.-P. (1998). Design of steel MRF connections before and after 1994 Northridge earthquake1Prepared for the International Conference on Advances in Steel Structures (ICASS), Hong Kong, 11–14 December 1996.1. *Engineering Structures*, 20(12), 1030–1038. [https://doi.org/10.1016/S0141-0296\(97\)00200-9](https://doi.org/10.1016/S0141-0296(97)00200-9)
- Shim, K. W., Monaghan, D. J., & Armstrong, C. G. (2002). Mixed Dimensional Coupling in Finite Element Stress Analysis. *Engineering with Computers*, 18(3), 241–252. <https://doi.org/10.1007/s003660200021>
- Shin, S. (2017, May). *Experimental and analytical investigation of panel zone behavior in steel moment frames* (Thesis). <https://doi.org/10.15781/T2K35MK5R>

Accepted: 2017-06-21T19:44:37Z

- Skiadopoulos, A. (2022). *Welded moment connections with highly dissipative panel zones for enhanced seismic performance of steel moment frames*. EPFL, Lausanne. <https://doi.org/10.5075/epfl-thesis-9513>
- Skiadopoulos, A., Elkady, A., & Lignos, D. G. (2021). Proposed Panel Zone Model for Seismic Design of Steel Moment-Resisting Frames. *Journal of Structural Engineering*, 147(4), 04021006. [https://doi.org/10.1061/\(ASCE\)ST.1943-541X.0002935](https://doi.org/10.1061/(ASCE)ST.1943-541X.0002935)
- Skiadopoulos, A., & Lignos, D. G. (2021). Development of Inelastic Panel Zone Database. *Journal of Structural Engineering*, 147(4), 04721001. [https://doi.org/10.1061/\(ASCE\)ST.1943-541X.0002957](https://doi.org/10.1061/(ASCE)ST.1943-541X.0002957)
- Skiadopoulos, A., & Lignos, D. G. (2022). Seismic demands of steel moment resisting frames with inelastic beam-to-column web panel zones. *Earthquake Engineering & Structural Dynamics*, 51(7), 1591–1609. <https://doi.org/10.1002/eqe.3629>
- Smith, M. (2019). *ABAQUS/Standard User's Manual, Version 2019*. Dassault Systèmes Simulia Corp.
- Yegian, M. K., Ghahraman, G. V., Gazetas, G., Dakoulas, P., & Makris, N. (1995). The Northridge Earthquake of 1994: Ground motions and geotechnical aspects. *Proc. 3rd Inst. Conf. on Recent Advances in Geotechnical Earthquake Engineering and Soil Dynamics*, 3, 1383–1389.
- Youssef, N. F., Bonowitz, D., & Gross, J. L. (1995). *A survey of steel moment-resisting frame buildings affected by the 1994 Northridge earthquake*. US National Institute of Standards and Technology.

12 Appendix

12.1 Design Summary

Design Summary

The eight-story, three-bay MRF design after adaptation is shown in Table. 1 (Interior).

Table. 1 Eight-story, three-bay MRF design.

Story / Floor	Column	Doubler Plate (in)	Beam
8/Roof	W24X94	8/16	W21X68
7/8	W24X131 W24X94	8/16	W21X68
6/7	W24X131	7/16	W24X76
5/6	W24X176 W24X131	7/16	W24X76
4/5	W24X176	6/16	W27X94
3/4	W24X192 W24X176	6/16	W27X94
2/3	W24X192	7/16	W27X102
1/2	W24X192	7/16	W27X102

The predicted $\tau_{cr} / 0.6f_y$ and $\gamma_{demand} / \gamma_y$ of the connections are shown in Fig. 1 and Fig. 2, respectively.

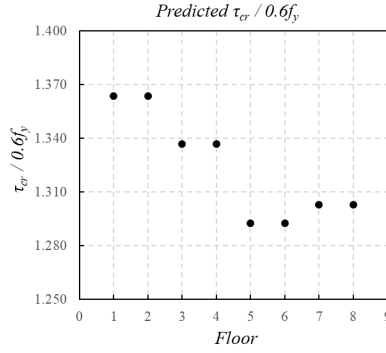


Fig. 1 $\tau_{cr} / 0.6f_y$ of connections at each floor

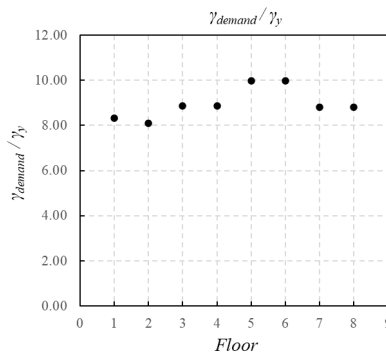


Fig. 2 $\gamma_{demand} / \gamma_y$ of connections at each floor

The eight-story, five-bay MRF design after adaptation is shown in Table. 2 (Interior).

Table. 2 Eight-story, five-bay MRF design.

Story / Floor	Column	Doubler Plate (in)	Beam
8/Roof	W24X84	5/16	W18X55
7/8	W24X94 W24X84	5/16	W18X55
6/7	W24X94	6/16	W21X62
5/6	W24X103 W24X94	6/16	W21X62
4/5	W24X103	8/16	W21X73
3/4	W24X131 W24X103	8/16	W21X73
2/3	W24X131	6/16	W24X76
1/2	W24X131	7/16	W24X76

The predicted $\tau_{cr} / 0.6f_y$ and $\gamma_{demand} / \gamma_y$ of the connections are shown in Fig. 3 and Fig. 4, respectively.

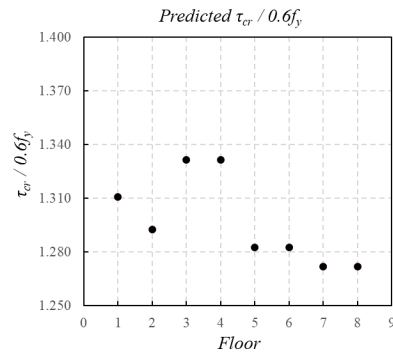


Fig. 3 $\tau_{cr} / 0.6f_y$ of connections at each floor

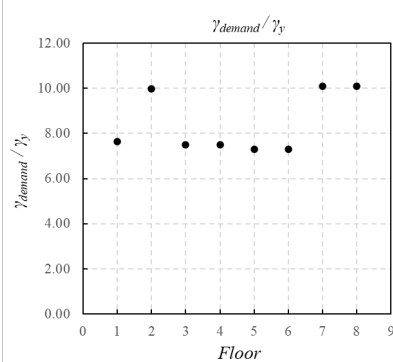


Fig. 4 $\gamma_{demand} / \gamma_y$ of connections at each floor

The Four-story, three-bay MRF design after adaptation is shown in Table. 3 (Interior).

Table. 3 Four-story, three-bay MRF design.

Story / Floor	Column	Doubler Plate (in)	Beam
4/Roof	W24X84	6/16	W18X60
3/4	W24X146 W24X84	6/16	W18X60
2/3	W24X146	7/16	W24X76
1/2	W24X146	7/16	W24X76

The predicted $\tau_{cr} / 0.6f_y$ and $\gamma_{demand} / \gamma_y$ of the connections are shown in Fig. 5 and Fig. 6, respectively.

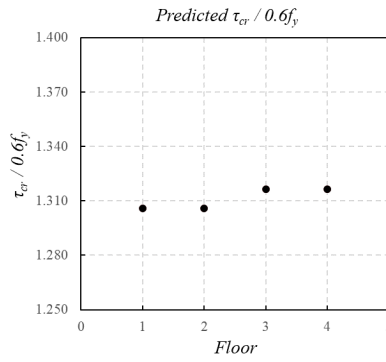


Fig. 5 $\tau_{cr} / 0.6f_y$ of connections at each floor

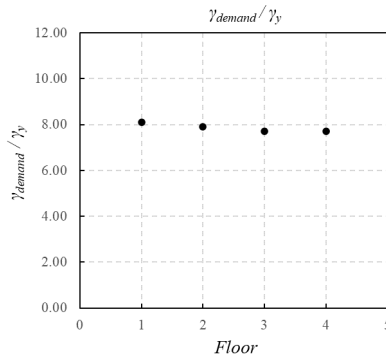


Fig. 6 $\gamma_{demand} / \gamma_y$ of connections at each floor